ALMA MATER STUDIORUM - UNIVERSITÀ DI BOLOGNA
CAMPUS DI CESENA
SCUOLA DI INGEGNERIA

CORSO DI LAUREA IN INGEGNERIA ELETTRONICA E TELECOMUNICAZIONI PER L'ENERGIA

SMART RADIO ENVIRONMENTS USING RECONFIGURABLE META-SURFACES

Elaborato in
Sistemi di Telecomunicazione LM

Relatore
Chiar.mo Prof. Ing.
DAVIDE DARDARI

Correlatori
Dott. Ing.
FRANCESCO GUIDI
Dott. Ing.
ANNA GUERRA

Presentata da
DEVIS MASSARI

Sessione II

Anno Accademico 2018-2019

Acronyms

EM electromagnetic

MTM metamaterial

MTS metasurface

RIS reconfigurable intelligent surface

IRS intelligent reflecting surface

IoT internet of things

IIoT industrial internet of things

BS base station

MS mobile station

DPS double positive materials

DNG double negative materials

SNG single negative structures

ENG epsilon-negative structures

MNG mu-negative structures

NIR negative index of refraction

LOS line-of-sight

NLOS non-line-of-sight

EIT electromagnetically induced transparency

PEC perfect electric conductor

PMC perfect magnetic conductor

SR spiral resonator

SRR split ring resonator

CSRR complementary split ring resonator

SR spiral resonator

EBG engineering bandgap material

PBG photonic bandgap material

PML perfect matched layer

CRLH composite right/left handed

MCSRR multi-stop complementary split ring resonator

SMCSRR square multi-stop complementary split ring resonator

CMCSRR circular multi-stop complementary split ring resonator

FPGA field programmable gate array

GRIN graded-index

GF Green's function

FSS frequency selective surfaces

RFID radio frequency identification

IC integrated circuit

MIMO multiple input multiple output

RCS radar cross section

SDN software defined networking

SDS software defined surface

SDR software defined radio

FP focus point

DoF depth of focus

W width of focus

FA focus area

NF near field

FF far field

OLDF orthogonal links density function

PG path gain

TE traffic engineering

CSI channel state information

Introduction

Nowadays we are experiencing a pervasive presence of wireless communication devices in the surrounding environments. Although their presence has led to the development of new communication technologies that promote mobility, the use of radio spectrum in recent decades has been intensive. The number of devices has increased considerably and with them the requests of users in terms of data rate. In fact, the propagation in environments characterized by obstacles, introduces multiple reflections called multipath, which can be more or less rich depending on the number of devices in communication or the density of obstacles. This type of phenomenon is particularly annoying because it causes interference that might dramatically reduce the system performance. Several techniques allow to face multipath, such as OFDM modulations, whereas other solutions permit to exploit it, like MIMO-5G systems.
Motivated by such considerations, in this work a new way of perceiving the propagation environment, by adopting metamaterials, has been tackled. Metamaterials are a new class of materials that, if properly programmed, can be exploited to obtain particular reflection coefficients. Moreover, they can also change the phase of the incident wave. In this scenario, assuming possible to install in the environment some surfaces composed of metamaterials called metasurfaces, customized reflection paths can be realized. This novel type of environment, which totally differs from the classic static concept perceived as an adversary, has been called intelligent. Hence, in the following we investigate the concept of smart radio environment, that is a completely programmable physical entity that allows the user to change the response of the channel arbitrarily.

Contents

Chapter 1

Metamaterials

1.1 Introduction

Metamaterials are a part of a very special and particular class of materials that exhibit an exotic behavior otherwise impossible to obtain with materials found in Nature [9]. electromagnetic (EM) metamaterials, or more simply metamaterials, are a very specific class of composite materials that can mimic known materials response or also create new responses not available in Nature.
In literature it is possible to find metamaterials (MTMs) for acoustic, elastic, mechanical, electromagnetic applications, and for every waves matter applications [3]. In this work will be discussed only the electromagnetic case.
Moreover MTMs can be engineered to get some unusual properties such as negative refraction, perfect lensing and invisible cloaking [8].

MTMs can be organized in planar (2D) and volumetric (3D) structures composed by periodic (homogeneous) or non-periodic (inhomogeneous) repetition of a MTM lattice called meta-atoms or unit cells [8]. One of the most important structure is the 2D one, and we refer to that as metasurfaces (MTSs).

In the following we will provide a general classification of actual MTMs solutions.

1.1.1 Classification

The purpose of MTMs is to manipulate EM fields that impact the surface, tailoring the response of the material to a desired application-dependent behavior [9].
In order to provide a classification, please refer to Fig. 1.1. As it can be seen, defining ϵ the permittivity and μ the permability, it is possible to find

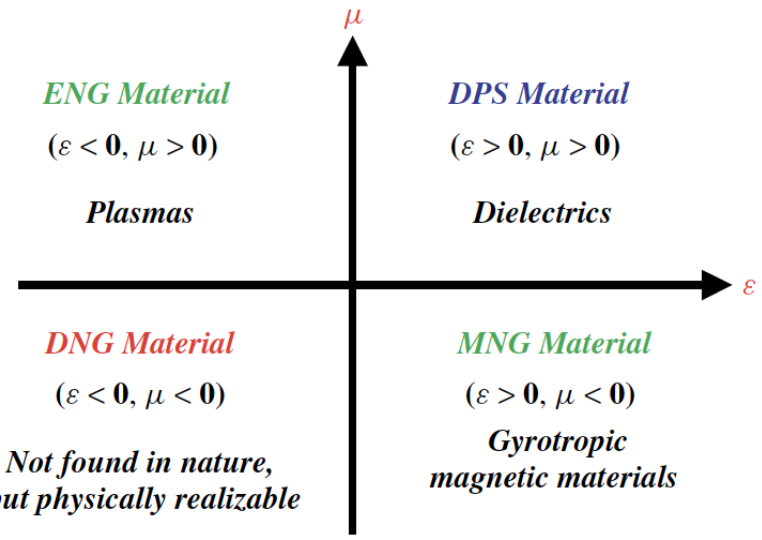

Figure 1.1: Material classification [9].

in Nature materials with positive permittivity and permability defined as double positive materials (DPS), epsilon-negative structures (ENG) which has negative permittivity or mu-negative structures (MNG) with negative permability and we refer to both as single negative structures (SNG).

On the contrary, MTMs belong to a class of materials characterized by a negative permittivity and permeability, namely double negative materials (DNG), that can not be found in Nature [8]. In literature, such DNG MTMs are usually referred to in several ways, such as Left Handed (LH), Backward-wave media etc [9], but thanks to their capability to provide a negative index of refraction (NIR), NIR MTMs is the most used one.

1.1.2 Electromagnetically induced transparency

electromagnetically induced transparency (EIT) concerns the capability of a medium to be transparent within a narrow spectral band centered on an absorption line and opaque in the other part of the spectrum [17].

The medium is set using a specific wavelength coming from a coupling laser which make the medium transparent. When the electric field coming from the coupling laser hits the medium, it becomes transparent. Then if a second field is emitted by a probe laser with a wavelength within a specific narrow band defined by the material, it can be observed that the probe field passes through the medium without any reflection or scatter phenomenon,

and that is true because the relative permittivity is $\epsilon_r = 1$ [15].

1.2 State of Art

A specific MTMs response is obtained by means of inhomogeneities. By introducing inhomogeneities in the MTMs propagation medium it is possible to modify the medium response and get a specific negative index of refraction [10].
According to the literature, it is possible to separate MTMs in Programmable and Non-Programmable, each of them further separable by means of the basic physical principle of operation:

- EIT MTMs [15, 19];
- Reflection MTMs [8, 28];

1.2.1 Mathematical Models

The most interesting feature for both programmable and non-programmableMTMs is the ability to perform negative values of permittivity and permability in order to realize NIR materials. In this section we show how the refractive index for DNG materials is derived. According to *Ziolkowsky and Heyman Theory*, it is possible to write [9]:

$$\sqrt{\epsilon} \triangleq \sqrt{\epsilon_r\epsilon_0 - j\epsilon"} \approx -j\left(\sqrt{|\epsilon_r\epsilon_0| + j\frac{\epsilon"}{2\sqrt{|\epsilon_r\epsilon_0|}}}\right) \tag{1.1}$$

$$\sqrt{\mu} \triangleq \sqrt{\mu_r\mu_0 - j\mu"} \approx -j\left(\sqrt{|\mu_r\mu_0| + j\frac{\mu"}{2\sqrt{|\mu_r\mu_0|}}}\right) \tag{1.2}$$

where ϵ_0, μ_0 are the vacuum permittivity and permeability, ϵ'', μ'' are the imaginary part of the complex permittivity and permability and ϵ_r, μ_r are the relative permittivity and permeability.

In particular, assuming ϵ, $\mu < 0$, and a small losses material, the Taylor series expansion has been used to approximate the expressions.

By using the same approach to the wave-number k and to the wave impedance η, it is possible to write

$$k \triangleq \omega\sqrt{\epsilon\mu} \approx -\frac{\omega}{c}\sqrt{|\epsilon_r\mu_r|}\left[1 + j\frac{1}{2}\left(\frac{\epsilon"}{|\epsilon_r|\epsilon_0} + \frac{\mu"}{|\mu_r|\mu_0}\right)\right] \tag{1.3}$$

$$\eta \triangleq \sqrt{\frac{\mu}{\epsilon}} \approx \eta_0\sqrt{\frac{|\mu_r|}{|\epsilon_r|}}\left[1 + j\frac{1}{2}\left(\frac{\mu"}{|\mu_r|\mu_0} - \frac{\epsilon"}{|\epsilon_r|\epsilon_0}\right)\right] \tag{1.4}$$

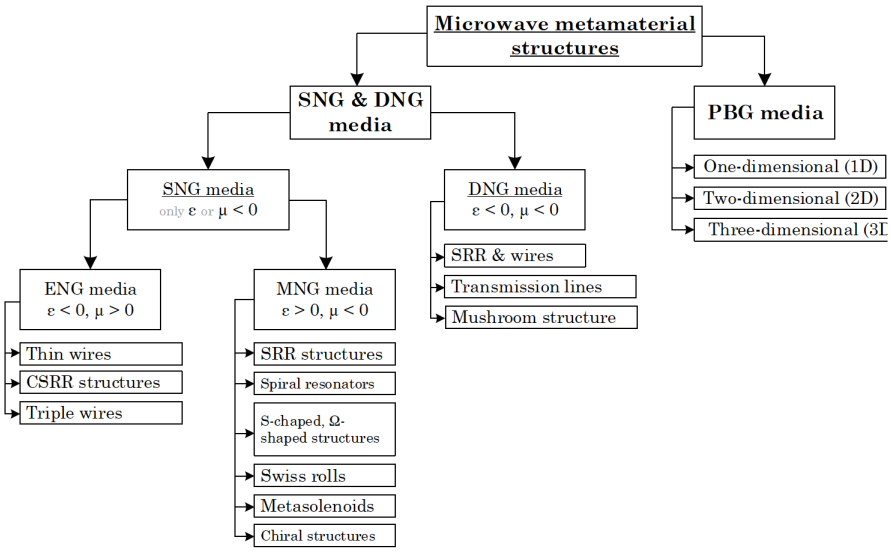

Figure 1.2: Generic classification of microwaves metamaterials constructions [5]

By injecting Equations (1.3) in Equation (1.4) we obtain

$$n \triangleq \frac{kc}{\omega} = \sqrt{\frac{\epsilon\mu}{\epsilon_0\mu_0}} = -\sqrt{\left[\left(|\epsilon_r||\mu_r| - \frac{\epsilon"\mu"}{\epsilon_0\mu_0}\right) + j\left(\frac{\epsilon"|\mu_r|}{\epsilon_0} + \frac{\mu"|\epsilon_r|}{\mu_0}\right)\right]}$$
$$\approx -\sqrt{|\epsilon_r||\mu_r|}\left[1 + j\frac{1}{2}\left(\frac{\epsilon"}{|\epsilon_r|\epsilon_0} + \frac{\mu"}{|\mu_r|\mu_0}\right)\right] \quad (1.5)$$

Notably, the real part of Equation (1.5) is negative, that leads to the definition of a NIR medium when DNG materials are exploited.

1.2.2 Non Programmable Structures

Non programmable structures (or non programmable MTMs) are made by static resonators which once printed on the board, their resonating properties can not be changed. Figure (1.2) shows a brief summary of the principal typology of MTMs. Concerning non-programmable structures, ad-hoc solutions have been proposed according to the entailed subwave-length structures [5, 10], and they comprise:

- SNG and DNG MTMs, which use several structures:
  - Thin Wires [ENG]

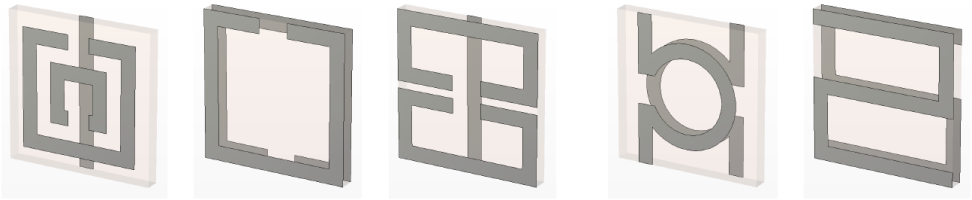

Figure 1.3: a) Edge-coupled SRR; b) Broadside SRR; c) Axially symmetric SRR; d) Omega SRR; e) S ring [23].

- split ring resonator (SRR) [MNG, DNG]
- complementary split ring resonator (CSRR) [ENG]
- spiral resonator (SR) [MNG]
- Swiss Roll [MNG]
- Metasolenoids [MNG]
- Chiral Structures [MNG]
- Shaped Structures (Ω, S) [MNG]
- Transmission Lines [DNG]
- Mushrooms Structures [DNG]

• engineering bandgap materials (EBGs) to control wave's phase front, also knew as Photonic Crystals or photonic bandgap materials (PBGs).

The length and the shape of the metal printed on the substrate, modifies the way the entire structure resonates at the designed frequency, in Figure (1.3) some examples are illustrated.

in order to provide an overview of the technologies briefly summarized above, a more detailed description of the main ones is provided in the following.

MNG structures: Split Ring Resonator (SRR)

SRRs are commonly used to realize MNG-structures because of their high-conductivity. The square and the circular versions are equivalent hence both are equivalently used. Notably, they exploit the fact that a time-varying magnetic field, incident to the rings, induces currents that create secondary magnetic fields reacting to the initial one, so that the MNG structure can

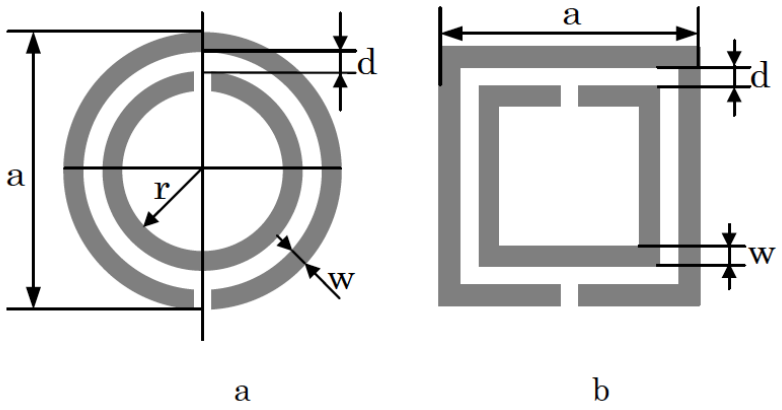

Figure 1.4: Example of a SRR MNG-material: a) round, b) square [5].

have aìì a positive or negative effective permeability μ_{eff} according to the following expression [5]

$$\mu_{eff} = 1 - \frac{\pi r^2/a}{1 + \frac{i2\sigma}{\mu_0 \omega r} - \frac{3d}{\pi^2 \mu_0 \omega^2 \epsilon_0 \epsilon_r^3}} \tag{1.6}$$

where r is the radius of the SRR, a represents the diameter or the maximum dimension of the structure, ω is the angular frequency and σ is the electrical conductivity.
The main drawbacks of SRRs are the narrow frequency band where $\mu_{eff} < 0$ and the high losses. The worst side effect of this SRRs is the anisotropic behavior In fact if the magnetic field is not incident to the structure, SRRs can not perform a negative effective permeability because they can not induce any magnetic field.
Some improvements have been studied and leads to a broadside solution (Fig. 1.5 h). Broadside-Coupled SRRs is built with two identical resonators at the both sides of a dielectric substrate where the ring gaps are at opposite sides. This structure permits an isotropic behavior of the resonator avoiding the main limit of classical SRRs [5].
SRRs compactness have been improved by new structures such as Spiral and S-shaped presenting an easier fabrication than SRRs [5].
It is worth noting new MNG-structures such as Swiss Roll and Metasolenoid have been designed to operate at different frequency ranges and different values of μ_{eff}.
Swiss Roll are suitable to operate at low frequency ranges ($f \approx 100MHz$) and they are disposed in array, whereas Metasolenoid can not have the same

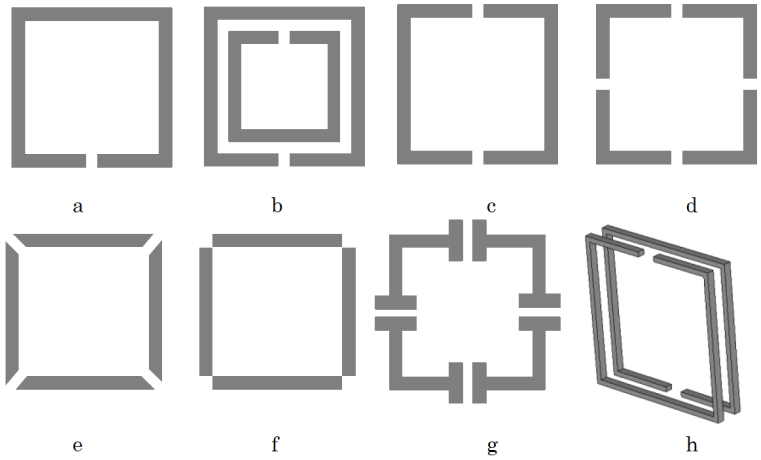

Figure 1.5: SRR evolution [5].

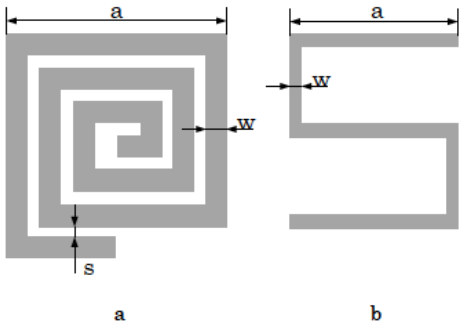

Figure 1.6: Example of MNG-materials: a) Spiral resonator, b) S-shaped [5].

wide bandwidth of SRRs, but they can achieve higher negative values of μ_{eff} [5].

MNG structures: Ω-shape

Ω-shape is an anisotropic structure that presents some advantages in terms of resonance frequency, that depends on the electric field orientation incident on the structure plane. Ω-shape are the most suitable solution to interact with linearly polarized plane waves useful for storing the largest amount of energy from the incident field. This structure is largely used for EM lenses fabrication [5].

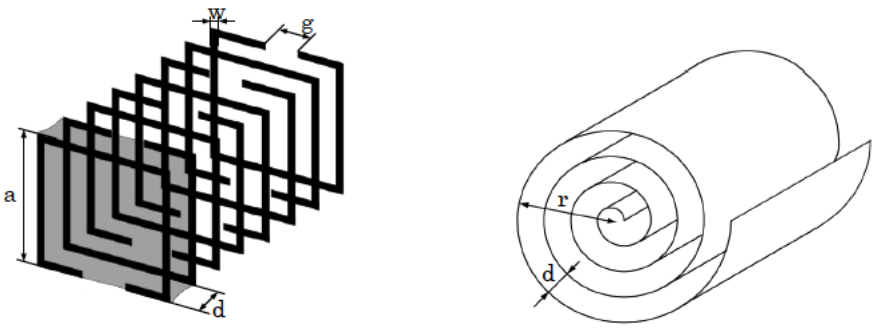

(a) Metasolenoid (b) Swiss Roll

Figure 1.7: Example of some alternative MNG-structures [5].

ENG structures: Thin Wires

Thin wire is the most common structure used to realize ENG-material and it consists of thin metal wires parallel positioned and embedded in a dielectric medium [5]. The permittivity of these structures is negative for $\omega < \omega_p$, where $w = 2\pi f$ and ω_p is related to the plasma frequency, and the effective permittivity is given by [5]

$$\epsilon_{eff} = 1 - \frac{\omega_p^2}{\omega\left[\omega - i\left(\omega_p^2 a^2 \epsilon_0\right)/\sigma\pi r^2\right]}. \tag{1.7}$$

ENG structures: Complementary Split Ring Resonator (CSRR)

CSRRs are the complementary structure of SRRs with metal inserted in the holes of the SRR structure. CSRRs belong to ENG-materials and it has a narrow frequency range near the resonance frequency and same as SRRs, CSRRs can have a round or squared shape as depicted in Fig. 1.8 [5].

DNG Metamaterials

According to [5], DNG metamaterials are divided in three different categories all depicted in Fig. 1.9

1) Thin Wires and SRRs;

2) Transmission lines;

3) Mushroom structure.

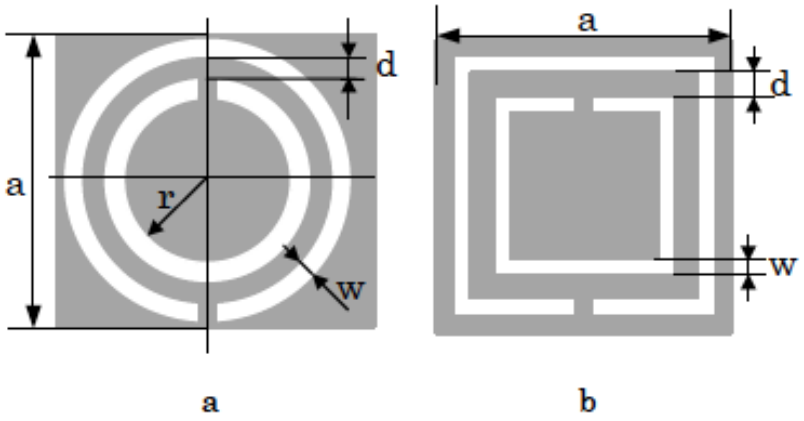

Figure 1.8: Example of a CSRR ENG-material: a) round, b) square [5].

Thin wires (Fig. 1.9a) are a combination of ENG and MNG structures in a way that it is possible to get the DNG behavior and obtain a negative index material. This structure has an important drawback in terms of operative frequencies inherited from SRRs that can be solved using more performing structures such as S-shaped, Metasolenoid or Spiral resonator [5].

Transmission lines (Fig. 1.9b) exploits the equivalent circuit method by means of parallel and/or shunt discrete components. By properly defining the values of the impedance and of the admittance, it is possible to obtain a customized response in terms of refraction index and for a given frequency. So this structure can behave like a positive or negative refracting index materials depending of the excitation frequency values and those type of materials are called composite right/left handed (CRLH) [5].

Mushrooms structures (Fig. 1.9c) are composed by an array of patches placed on a dielectric substrate and connected to the ground through a via hole realized with a PIN diode. This structure can operate at millimeter and sub-millimeter waves, and the frequency behave can be modified by switching on or off the diodes. [5]

1.2.3 Programmable Structures

One of the most relevant objective is the possibility to realize a programmable MTS. Programmable MTS, as well known as tunable or active MTS, can change the way they react to an electromagnetic field through the setting of some input signals.

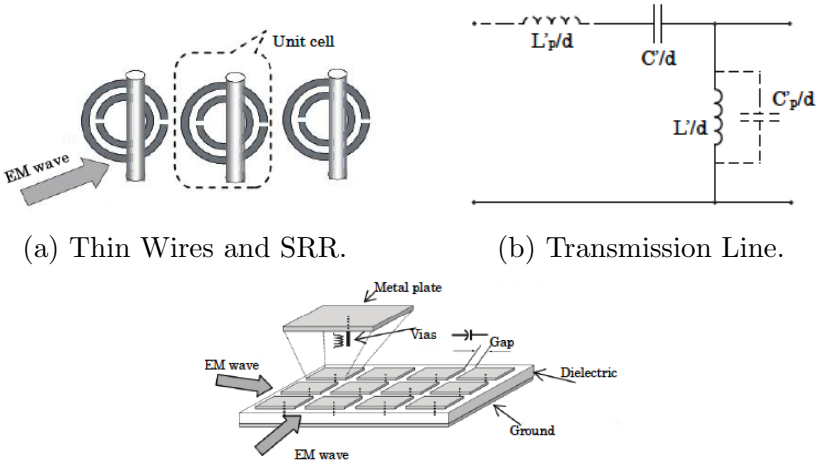

(a) Thin Wires and SRR. (b) Transmission Line.

(c) Mushroom

Figure 1.9: Example of the most common DNG metamaterials [5].

EIT-Based Metasurfaces

Literature [8, 15, 19, 28] proposed a surface capable to become transparent to specific frequencies and opaque to others. This particular behavior is referable to an EIT principle. This turns out to be useful to transform an antenna in a steerable antenna by programming every single subwavelength structures which build up the MTS itself [15].
The objective is to create a structure capable of behaving like a transparent medium at a fixed frequency and like a lossless perfect matched layer (PML) when hit by frequencies belonging to the opaque band [15]. The advantage of this solution is the possibility to place the surface in the middle of transmitter and receiver antennas, by modifying the electromagnetic field directly from the output of the transmitter. Several structures have already been proposed in the literature [15,19], many of them exploiting varactors, and few examples are reported in Fig. 1.10. By properly setting the varactor, the junction capacitance changes and the subwavelength structure (or unit cell) modifies its behavior accordingly [15, 19].

In the first case (Fig. 1.10a) the unit cell measures are $t = 1$ mm, $w = 0.8$ mm, $q = 4.35$ mm, $v = 5.95$ mm, $s = 3.15$ mm, $m = 12.1$ mm, $g = 2.2$ mm and $P = 12.5$ mm and the cell can be repeated in a $M \times N$ matrix. The MTS can provide a beam steering control up to 30° [15] as shown in Fig. 1.11b by programming the unit cells by row.

In the second case (Fig. 1.10b) the unit cell acts like a memory, trapping and then releasing the electromagnetic field inside the resonator.

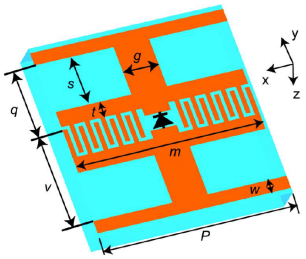

(a) Unit cell 1 (@3.985GHz).

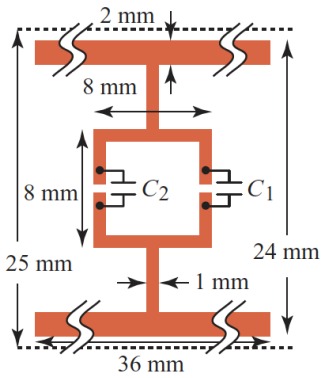

(b) Unit cell 2 (@1.440GHz).

Figure 1.10: Examples of subwavelength programmable structures [15, 19].

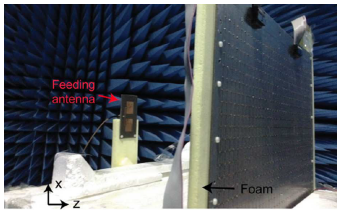

(a) Test condition

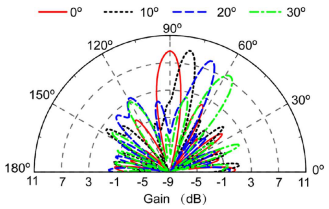

(b) Gain pattern Unit cell 1 [15]

Figure 1.11: Beam steering result obtained by means of Unit Cell 1

Fig. 1.12a reports the modulated signal of a 3 layers metastructure where each layer is a MTS consisting of a matrix of cells, where according with [19], each layer is separated from the others by a 7 cm gap to avoid undesired coupling. The transmitted power is measured through the waveguide.
Fig. 1.12a show the part of the electromagnetic energy is stored in the unit cell and then released as a consequence of the alternate of *EIT on* and *EIT off* states.
The retrieved delay is tunable as we can see in Fig. 1.12b, and can assume different values [19].

Reflection-Based Metasufraces

Differently from the EIT, this method allows to modify the electromagnetic field thorough the reflection on a MTS composed by a lattice of single MTMs

(a) Memory Effect of a single unit cell

(b) Tunable Delay

Figure 1.12: EIT based metamaterial [19]

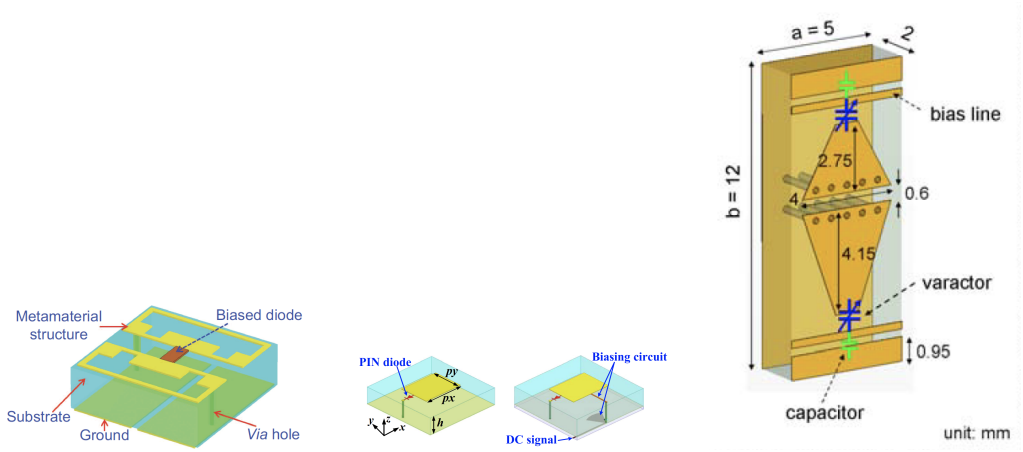

(a) Unit cell 1.

(b) Unit cell 2.

(c) Unit cell 3.

Figure 1.13: Examples of subwavelength programmable structures [8, 11, 28].

unit cells. Each unit cell, with size smaller than a wavelength, can perform several phase responses as a function of the adopted n-bit coding [8].
Unit cells are realized by means of discrete components like varactors and the shape of a single cell can be modified [8, 11, 28].

By the repetition of those single structures, different MTS are obtained and as a function of the coding strategy adopted, different behavior are performed such as *Polarization Control*, *Scattering* and *Focusing/Beam Forming* (Fig. 1.14). [8, 28]

By means of unit cells called *Digital Metamaterial*, several coding strategies can be realized: [8]

- *1-bit coding*: The unit cell can perform a 0 and π phase response associated to the digits "0" and "1", respectively;

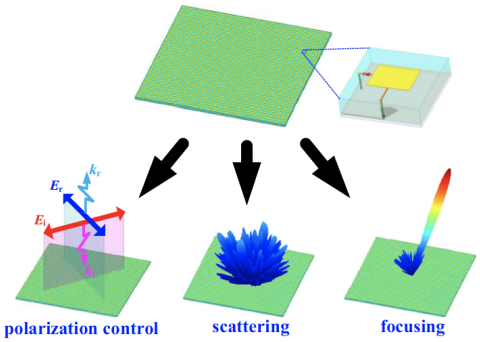

Figure 1.14: Example of 1-bit coding multiple functions metasurface [28].

- *2-bit coding*: The unit cell can perform a 0, $\frac{\pi}{2}$, π and $\frac{3}{2}\pi$ phase response associate to the sequences '00', '01', '10' and '11' respectively;

- *n-bit coding*: The concept is extensible to n coding dimension getting 2^n codes. The larger is n, the larger is the number of available degrees of freedom to control the electromagnetic field.

In [8], the system composed of a MTS of *Digital Metamaterial* and a field programmable gate array (FPGA), as it is shown in Fig. 1.15 has been defined as "Programmable metamaterial". With the programmable metamaterial it is possible to obtain a fully programmable structure able to manipulate the electromagnetic wave through its reflection. [8]

In this chapter we have seen the main categories of MTMs realized which will be of considerable importance in realizing some new applications. Some of the novel works which make use of MTMs have been chosen and discussed in the following in order to give a general overview of the state of the art.

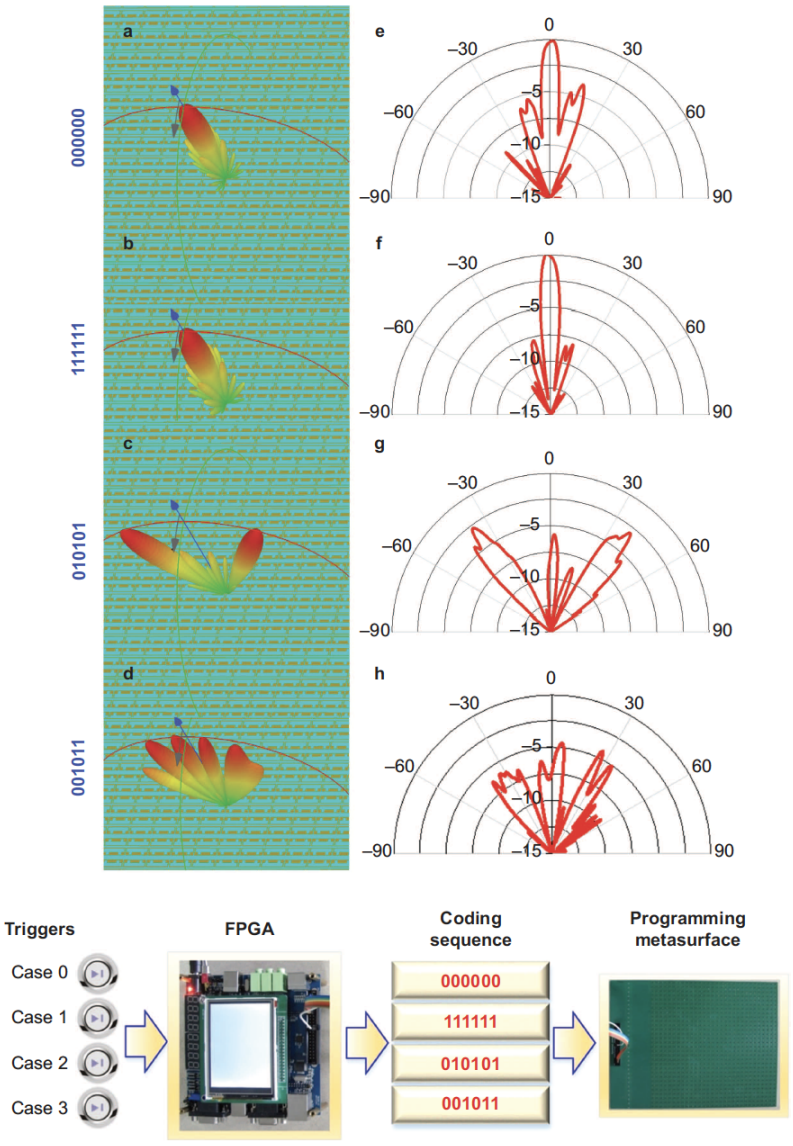

Figure 1.15: Example of programmable metamasurface [8] @8.6GHz as central frequency in a 30×30 structure with each unit is $(6 \times 6 \times 2)$ mm^3.

Chapter 2

Applications with Metamaterials

2.1 Mathematical Operations using Metamaterials

One of the most interesting and investigated functionality is the possibility to create some metastructures capable of manipulating the electromagnetic waves and perform some desired mathematical operations [3, 14, 18, 26].
The reason why this application turns to be so interesting, is because complex mathematical operations are performed with electronic programmable devices that first need the presence of dedicated electronics to convert electromagnetic waves into electrical analog signals and then in digital signals. However this chain leads to a processing overhead, and it would be preferable to perform some pre-processing operations directly on the incident EM wave, to improve the elaboration speed and reduce the power consumption [14].
In the following we will see by the theoretical prospective, how to use MTMs to perform some of the most common post-processing operations directly on the EM field. Most of the approaches present in the literature refer to [3], that focuses on two different MTM implementations that allow to attain the same result.

Two proposed implementations make use of different layers of MTSs. The first one called MTSs Approach uses a thin planar metamaterial block to perform operation in the spatial Fourier Domain. The second one called Green's function (GF) Approach uses a multilayered MTM slab to realize a desired Green's Function. [3]

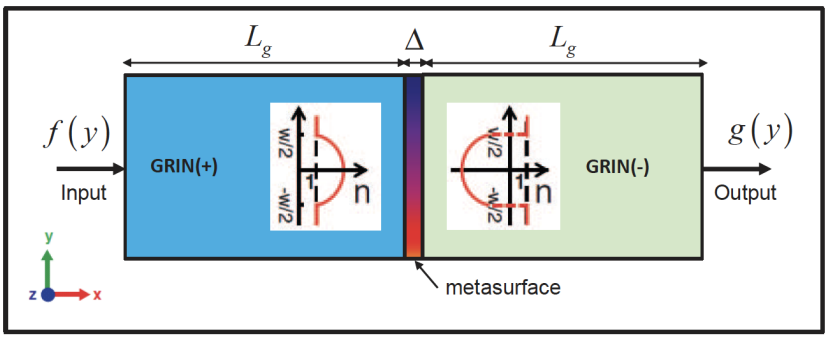

Figure 2.1: Example of a Single MTS layer structure [26].

2.1.1 Single Layer: MTS Approach

This approach considers operations in the spatial Fourier domain in the form [3].

$$g(y) = \int f(u)G(y-u)du \tag{2.1}$$

where:

- $f(y)$ is an arbitrary input field distribution;
- $G(y)$ is a kernel function that implements a chosen operator in Fourier Domain;
- $g(y)$ is the output field distribution.

A tailored single metasurface layer is positioned in the middle of two bigger blocks called graded-index (GRIN). Those blocks realize the Fourier Transform (GRIN+) and the Inverse Fourier Transform (GRIN-) according to the optical lenses theory [3].

Then after the Fourier Transform, the Eq. (2.1) turns to be:

$$\tilde{g}(k_y) = \tilde{f}(k_y)\tilde{G}(k_y). \tag{2.2}$$

Every single GRIN blocks has a parabolic permittivity function (see Fig. (2.1)) that can be expressed as Eq. (2.3) whereas the permeability remains constant, i.e., $\mu = \mu_0$.

$$\epsilon(y) = \epsilon_c \left[1 - \left(\frac{\pi}{2L_g}\right)^2 y^2\right] \tag{2.3}$$

where ϵ_c is the permittivity at the central plane of the GRIN and L_g is the characteristic length and it is also indicated in Fig. (2.1).

The MTS Approach with an-hoc design of volumetric parameters ϵ_{ms} and μ_{ms} can perform several mathematical operations like first-order derivative, second-order derivative, Integration and Convolution [3].

First-Order Derivative

$$\tilde{G}(k_y) = \frac{iy}{(W/2)}$$

$$\frac{\epsilon_{ms}(y)}{\epsilon_0} = \frac{\mu_{ms}(y)}{\mu_0} = i\left(\frac{\lambda_0}{2\pi\Delta}\right)\ln\left(\frac{-iW}{2y}\right) \tag{2.4}$$

where W is the width of the MTS, Δ is the MTS's thckness and λ_0 is the wavelength in free space.

Second-Order Derivative

$$\tilde{G}(k_y) = \left[\frac{iy}{(W/2)}\right]^2$$

$$\frac{\epsilon_{ms}(y)}{\epsilon_0} = \frac{\mu_{ms}(y)}{\mu_0} = i2\left(\frac{\lambda_0}{2\pi\Delta}\right)\ln\left(\frac{-iW}{2y}\right) \tag{2.5}$$

where W is the width of the MTS, Δ is the thickness of the MTS and λ_0 is the wavelength in free space.

Integration

Assuming an arbitrary normalizing length $d = 1$:

$$\tilde{G}(k_y) = \frac{d}{iy}$$

$$\frac{\epsilon_{ms}(y)}{\epsilon_0} = \frac{\mu_{ms}(y)}{\mu_0} = \begin{cases} i\left(\frac{\lambda_0}{2\pi\Delta}\right)\ln\left(\frac{iy}{d}\right), & \text{if } |y| > d. \\ -\left(\frac{\lambda_0}{4\Delta}\right)\operatorname{sgn}\left(\frac{y}{d}\right), & \text{if } |y| < d. \end{cases} \tag{2.6}$$

where W is the width of the MTS, Δ is the thickness of the MTS, λ_0 is the wavelength in free space and d is the gap between the layer composing the MTS slab.

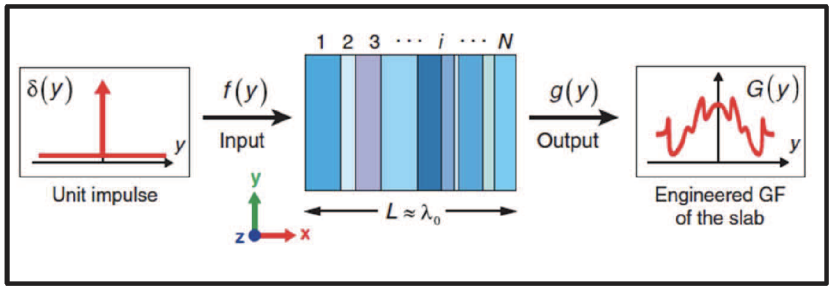

Figure 2.2: Example of a Green Function multilayer structure [26].

Convolution

$$\begin{cases} \tilde{G}(k_y) = \text{sinc}\left(\frac{W_k y}{2s^2}\right), \\ s = \sqrt{\frac{\lambda_0 L_g}{\pi^2 \sqrt{\frac{\epsilon_c}{\epsilon_0}}}} \end{cases}$$

$$\frac{\epsilon_{ms}(y)}{\epsilon_0} = \frac{\mu_{ms}(y)}{\mu_0} = i\left(\frac{\lambda_0}{2\pi\Delta}\right)\ln\left(\frac{1}{\text{sinc}\left(\frac{W_k y}{2s^2}\right)}\right) \tag{2.7}$$

where W is the width of the MTS, Δ is the thickness of the MTS and λ_0 is the wavelength in free space.

2.1.2 Multilayered: GF Approach

This second approach avoids the need of going into the Fourier spatial domain and uses a multilayered MTM slab transversely homogeneous, which directly implements a GF. So the GRIN blocks are no more necessary.
It is possible to define a particular set of functions so that, in order to realize a second-order derivative, Eq. (2.1) becomes [3, 26]:

$$g(y) = \frac{d^2 f(y)}{dy^2} = \int f(u)\delta''(y-u)du \tag{2.8}$$

where $\delta''(y)$ is the second spatial derivative of the Dirac delta function.

In this case the purpose is to tailor the transmission coefficient for impinging plane wave as a function of the transverse wavenumber k_y by means of several thin metasurfaces layers with overall thickness equal to the wavelength [3].
Fig. (2.2) shows an example of a real implemented impulsive response of a

multilayered structure. This leads to the possibility to realize any impulsive response that allows to reduce the signal processing complexity at the hardware level.

2.2 Chipless RFID

Chipless radio frequency identification (RFID) has been introduced in order to further reduce the cost of RFID tags which are still much expensive to be used in practical applications. [7, 12]
The acronym RFID identifies a communication system largely used for identification purposes. RFIDs are defined by the presence of two devices, the Reader and Tag which interact together by means of EM field in both near field (NF) and far field (FF) conditions. To interrogate the tag, the reader emits an EM wave, the tag answers back to the reader rejecting the same wave and applying a code internally storage. Then the reader can understand the tag identity simply reading the code impressed by the tag itself. The principal advantage in RFID communication is the low amount of energy used by the devices. The drawback in RFID is due to integrated circuits (ICs), as a matter of fact ICs are the most expensive part of the device and the most important because are used to storage all the tag informations. Nowadays market aims to have programmable devices where to encode information without the use of ICs [7].
Chipless RFID promises reducing fabrication costs and providing convenience to the consumer [12].

Chipless RFID tags can be realized by using MTMs. In fact MTMs can react in different ways depending on the excitation frequencies. It is possible to create structures able to resonate at different frequency and, to exploit this behavior, several technology has been implemented. In particular, the solutions herein reported account for variations of the radar cross section (RCS) [7, 12] and, thanks to the adoption of MTMs, it is possible to realize a multi resonate material which can be used to store data.

In the following we propose two solutions which offer the possibility to realize totally passive tags without the use of ICs simply exploiting the MTM's characteristic to behave differently to exciting frequencies.

2.2.1 Solution 1: Multi resonant SRR tag

Recently, it has been proposed the possibility to realize chipless tags by means of a dielectric substrate covered by a matrix of SRRs, where each rings resonate at a specific frequency [7]. In this way the reflection coefficient can

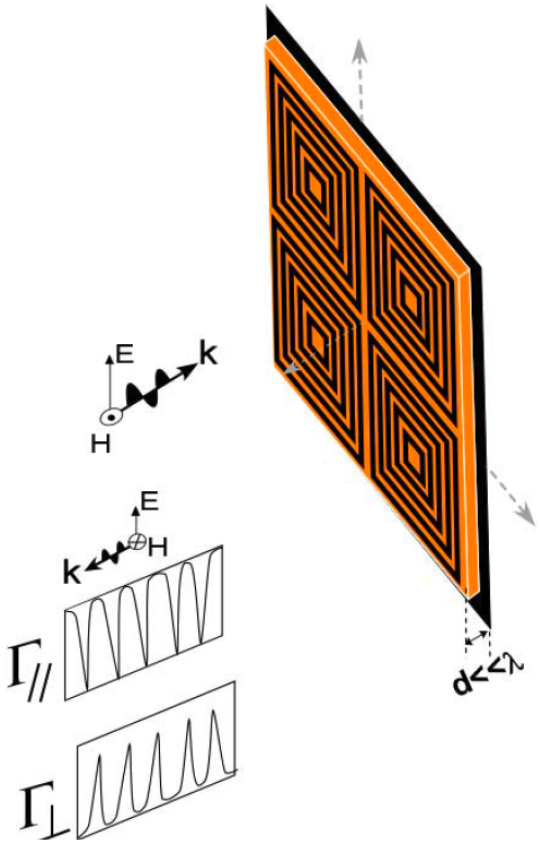

Figure 2.3: Layout of the 10 bit RFID tag [7].

exhibit variations along all the bandwidth and and the bits '1' and '0' are associated to the presence or not of an absorption peak, respectively.

The variable reflection coefficient leads to a variable RCS as function of the excitation frequency, and the information in this structure can be stored in two ways [7]:

- exploiting the co-polar component of the reflection coefficient;

- exploiting the cross-polar component of the reflection coefficient.

The tag reading range is given by

$$R_{range} = \sqrt[4]{\frac{G_T G_R \lambda^2 \sigma P_T}{(4\pi)^3 P_{min}}} \tag{2.9}$$

where G_T and G_R are the transmitter and receiver antenna gain respectively, λ is the wavelength, P_T is the transmitted power, P_{min} the sensitivity of the receiver and σ, the RCS is given by

$$\sigma = \frac{4\pi L^2 w^2}{\lambda^2}. \tag{2.10}$$

It is worth noting that the tag reading range can be expressed as [7]

$$R_{range} = \sqrt[4]{\frac{G_T G_R L^2 w^2 P_T}{(4\pi)^2 P_{min}}} \tag{2.11}$$

where L and w are the length and the width respectively of a metallic plate with the same size of the tag, used to estimate the RCS. There is no dependance on the operating frequency, but only on the tag physical size.

In the following, we describe how the co-polar and the cross-polar components are exploited.

Co-polar Reflection coefficient

Defining a MTM absorber as an extremely thin structure able to dissipate all the incoming EM power coming from all the incident angles at a single frequency, assuming possible to obtain this characteristic using a SRR, a matrix of SRRs can be used to realize an absorber in a range of frequencies. If all the resonators are activated, an all-zero sequence is encoded. By turning off some of the resonators is possible to create a structure resonant to specific frequencies, hence some peaks due to the co-polar reflections appear. Turning on or off the SRRs a code can be created [7].
Fig. (2.4) shows an example of co-polar reflection tag composed by a 3×3 SRRs array with dimensions (4.5×4.5) cm, where for each designed resonant frequency the normalized reflection coefficient has a down peak. The reflection coefficient is normalized with respect to the scattering level of a PEC plate of the same size of the tag [7].

Cross-polar Reflection coefficient

This case take in account the cross-polar reflection. It can be exploited using the same SRRs structure, but adding a ground plane on the back of the tag. As the ground plane become larger, the co-polar reflection coefficient goes to zero. Fig. (2.5) shows the cross-polarization which is not affected by the presence of ground plane. Using SRRs engineered to react to the cross-polar component of the electric field, the same result is obtained. As a matter fo

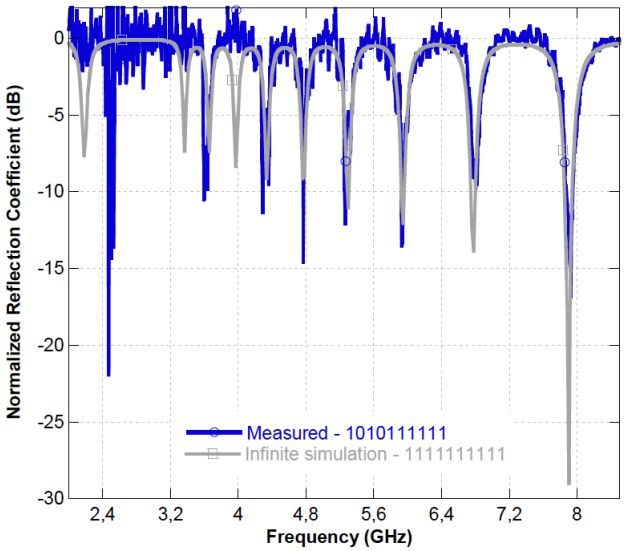

Figure 2.4: Example of measured Co-polar Reflection coefficient vs Numerical simulation of a 3×3 10 bits tag [7].

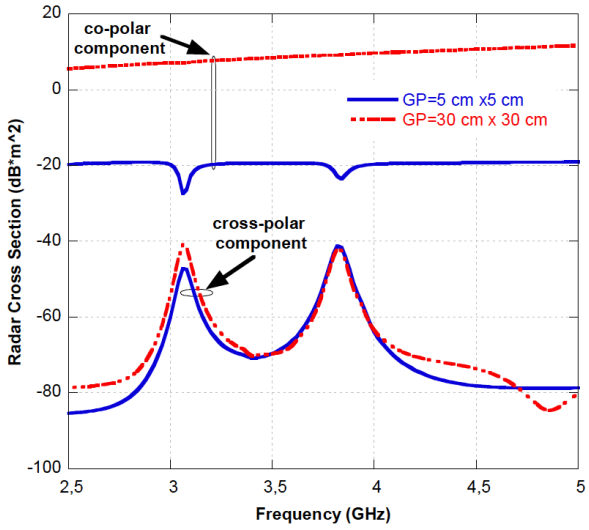

Figure 2.5: Cross-polar vs co-polar reflection coefficient of a 3×3 tag placed over a metallic ground plane with variable dimensions [7].

fact, Fig. (2.6) shows that exploiting cross-polar reflection, a similar working tag can be obtained [7].

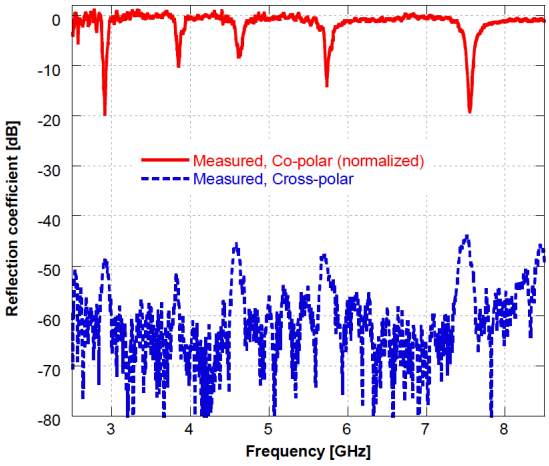

Figure 2.6: Example of No-Normalized Cross-polar reflection coefficient measured on a 5 bits (11111) 3×3 tag placed over a metal ground plane [7].

2.2.2 Solution 2: Multi resonant Gap CSRR tag

Recently, a new chipless tag solution, called *Frequency Shifting Approach* has been proposed [12]. Differently from the Solution 1, Solution 2 uses CSRRs instead of SRRs and a new class of MTMs called multi-stop complementary split ring resonator (MCSRR).
All the SRR has an interruption in the metallic ring called gap, the same structure is exploited in CSRRs which use two SRRs with gap at opposite sides. This new class of MTMs differentiates from CSRRs due to the insertion of a variable gap in the resonator. Such a variation allows to change the resonance frequency of the resonator, and hence the resonator can switch between more resonant frequencies.
MCSRRs can be further divided in two more structures: Square (SMCSRR) and Circular (CMCSRR) where for each ring a specific resonance frequency is excited. The electrical length of the rings can be determined by

$$L_{no} = \frac{c}{2f\sqrt{\epsilon_{eff}}} \tag{2.12}$$

where L_{no} is the length of *no* ring for both square and circular MCSRRs.

As an example, four new configurations are introduced in [12], thanks to the adoption of four gaps with a-priori fixed dimensions, where each gap length in each ring is coded by 2 bits (see Figure 2.7).

Table 2.1 shows how gap widths are chosen to perform the 200 MHz frequency shift. As an example, assuming the number of SRRs in MCSRR

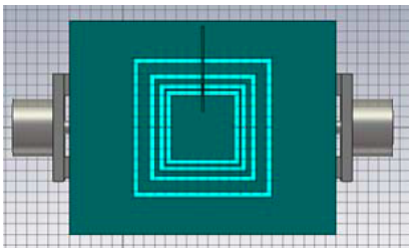

(a) Square Multi-stop Complementary Split Ring Resonator (SMCSRR)

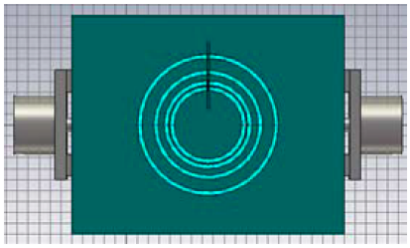

(b) Circular Multi-stop Complementary Split Ring Resonator (SMCSRR)

Figure 2.7: Examples of new class of resonators studied. It is worth noting the gap positioned in the upper part of both resonators [12].

Coded Bits for a SMCSRR		
Gap Width [mm]	**Frequency Range [GHz]**	**Coded Bits**
0.25	2.50 - 2.70	00
2.00	2.75 - 2.95	01
5.00	3.00 - 3.20	10
8.00	3.25 - 3.45	11

Table 2.1: Coded bits as function of the gap width and frequency ranges [12].

is 4 and for each of the resonators 2 bits can be coded, the total number of bits we can store in the MCSRR is 8 [12].

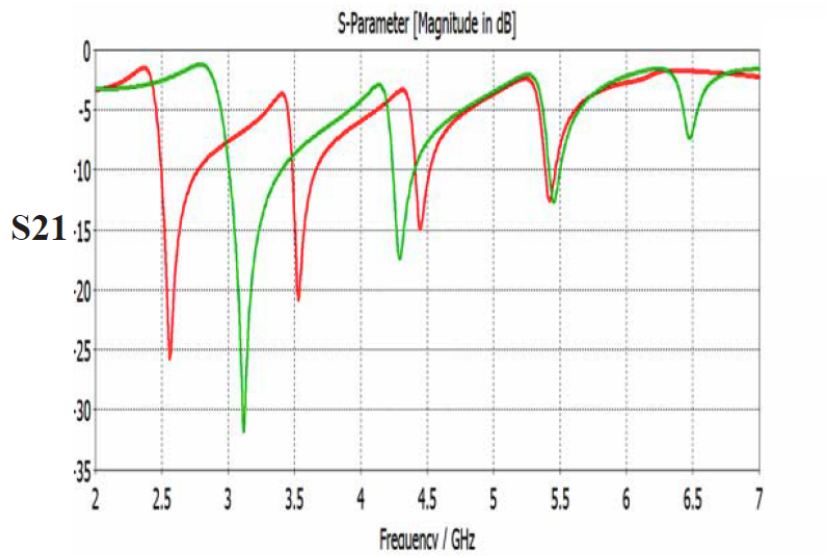

(a) SMCSRR and CMCSRR resonance frequencies

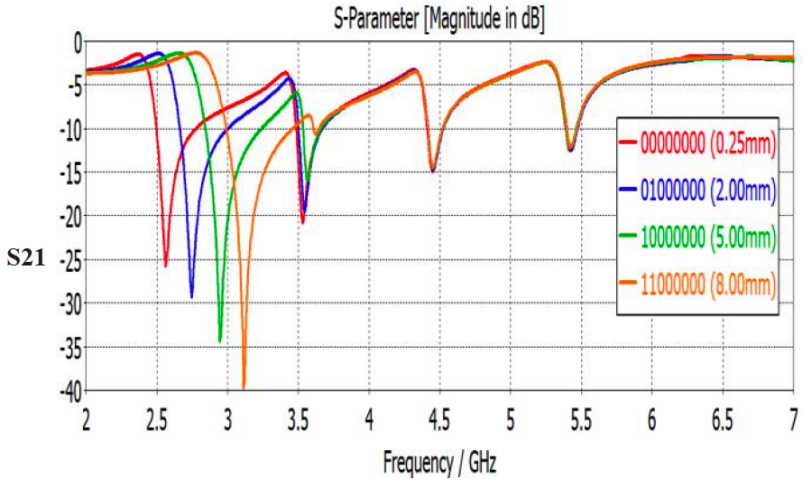

(b) Multi-Gap effect in a SMCSRR

Figure 2.8: Differences between MCSRRs return loss with and without gap [12].

Chapter 3

Propagation Environment

3.1 Current Radio Environment Models

The physical environment alters significantly the radio propagation thus heavily modfying the communication channel response. In fact, after the communication theory, the environment has been treated as a passive entity that can severely affect the performance. In this sense, the communication methods so far deployed, usually rely on three main postulates [22]:

- The environment is usually perceived as an "unintentional adversary" to communication and information processing.

- Only the end-points of the communication network are usually optimized.

- Wireless network operators have usually no control of the environment.

One of the most commonly used wireless networks is the cellular network. The fundamental characteristic of cellular networks is the user's mobility and thus they are not uniformly distributed in the environment.
This results in having some base stations overloaded and others underutilized. This behavior is the main issue affecting wireless network. [22].

In order to overcome this problem, some techniques have been developed:

- Load Balancing;

- Densification of Base Stations;

- MIMO schemes.

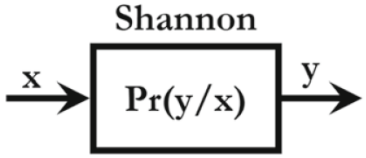

Figure 3.1: Communication model for radio environment proposed by Shannon [22].

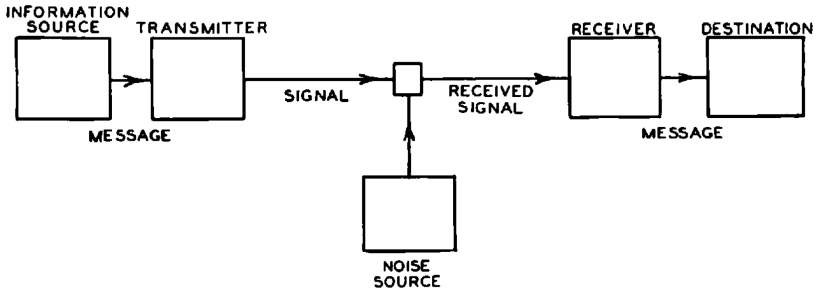

Figure 3.2: Schematic diagram of a general communication system [25].

3.1.1 Shannon's Model

Shannon formulated his theory in terms of transition probability $Pr(Y|X)$ that represent (see Fig. 3.1) the probability to get the Y channel response when the source is X [22].

According with Shannon's work [25], the communication channel has been modeled as a propagation medium affected by noise and by this assumption the communication link can be represented with the block scheme of Fig. (3.2).

A deeper discussion on Shannon's work on the Mathematical Theory of Communications can be found in [25]. Here it is important to notice that the environment has been characterized as a passive entity that communication applications must face up to.

3.1.2 Wiener's Model

Wiener formulated a really wide theory on feedback loops which are used as a regulation mechanism of the entire system. As depicted in Fig. (3.3), the output has been fed back to the input, therefore the communication model can take into account the output which turns out to be useful when a new

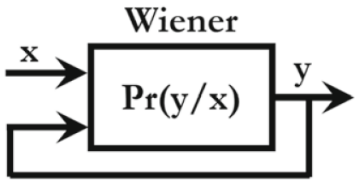

Figure 3.3: Communication model for radio environment by Wiener [22].

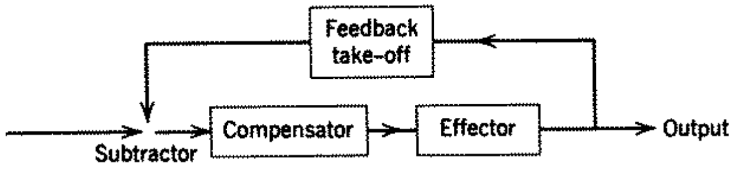

Figure 3.4: Schematic diagram of a feedback loop [27].

signal has been placed in input [22].

Fig. (3.4) represents possible arrengement discussed in Wiener's work [27]. The *Effector* block mimics the environment behavior and the *Compensator* block must compensate the medium response and, according to WIener's, it has to predict and fix the *Effector*. Indeed, the *Feedback Loop* must anticipate the *Effector* response to the *Compensator* in order to overcome the delay of the *Compensator* itself [27].

3.2 Next generation Radio Environment Model

Nowadays there is a high traffic demand due to the pervasive presence of electronic devices required to exchange a large amount of data. In this sense, an interesting opportunity is offered by moving up in the frequency spectrum, where there are several unused bands, especially at 60 GHz. This translates into shorter wavelengths, in the order of millimeter or sub-millimeter wave, however these frequencies are more susceptible to blockages from large-size structures on the radio path.
Furthermore, this problem is even more pronounced for mobile in dense urban environment where the propagation path is way more dynamic [21]. As a matter of fact, introducing mobility in the system, the relative position between transmitter and receiver changes. For this reason the conditions of the channel are not static but dynamic. Furthermore, considering the prop-

agation environment occupied by obstacles, the transmitter and receiver can be in non-line-of-sight (NLOS) condition and it introduces fading in the link. Finally, the presence of obstacles produces multiple reflections in the environment. These delayed repetitions of the signal can introduce undesirable effects during the reception. This phenomenon is known as multipath.
In order to manage the mobility, the first approach is to deploy a large number of relay station in the area of interest to enhance the signal received from a mobile user. Relays can turn a single NLOS link, into a multiple line-of-sight (LOS) links. Nevertheless, this solution implies a high cost due to such dense deployment as well as a high power consumption due to the need of dedicated power sources with the related circuitry for receiving, processing and transmitting signals. Notably, the drawback of this approach is that the network complexity might explode [21].

Recently, in order to overcome the aforementioned issue, it has been explored the possibility to deploy in the environment some passive electromagnetic mirrors also identified as passive non-reconfigurable specular reflectors, that exhibit the same behaviour of relays without requiring ad-hoc power sources. Nevertheless this totally passive solution is not useful in high dynamic environments because it has a static configuration. A modification is needed and reconfigurable intelligent surfaces (RISs) have been introduced to transform the static radio environment into a Smart Radio Environment by consuming a lower amount of energy than the actual relays based solutions [21].

3.2.1 Reconfigurable Intelligent Surfaces (RISs)

RIS are often referred to as software defined surfaces (SDSs) in analogy with the concept of software defined radio (SDR), hence a RIS can be viewed as an SDS whose EM response is programmed by software [4].
Usually, RISs are composed by several programmable MTSs that are classified in two categories:

- PIN Diode based MTSs, that are controllable by PIN Diodes. By turning on/off a particular configuration of PIN diodes, the user can change the reflection coefficient of the MTS. A matrix of such MTSs realizes an intelligent reflecting surface (IRS) [4].

- Varactor based MTSs, that are controllable by Varactors. Operating like this, the MTSs can still vary the reflection coefficient, but can also vary the phase response of the wave impinging on it. A matrix of those MTSs realizes a RISs [4].

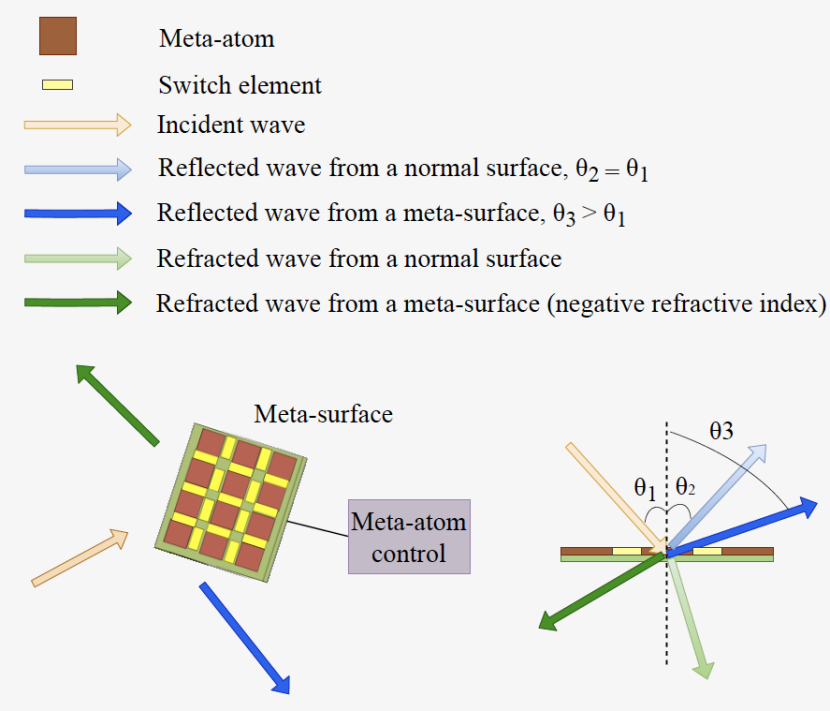

Figure 3.5: IRS working principle [21].

To this purpose, Fig. (3.5) report an example of an IIRS, however RISs, on the contrary ofIRS, are not only able to reflect the EM field, but they can change the phase and the shape of electromagnetic wave by reflecting and refracting the impinging signal to anomalous direction not predicted by the Snell's Law [21].

Resuming, the power of RISs is to turn the environment into a programmable and partially deterministic space named as smart radio environment [22]. RISs are artificial surfaces capable of altering the electromagnetic propagation of waves impinging on it. By covering obstacles (e.g. buildings, walls, furniture) already present into the propagation environment, several new combinations in the propagation of EM waves are added with the consequence that better communication performances could be obtained.

3.2.2 Smart Radio Environments

As previously anticipated, smart radio environments are defined as a radio environment that is turned into a smart reconfigurable space that plays an active role in transferring and processing information, and that makes more reliable the exchange of data between transmitters and receivers [22].

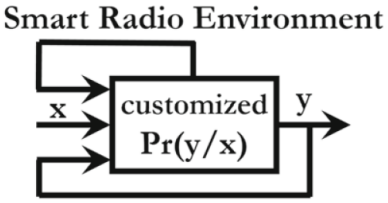

Figure 3.6: The new communication model for smart radio environment [22].

For this purpose configurable RISs can be used to perform a new communication paradigm able to sense the environment conditions and change its own configuration in order to realize a better communication between transmitters and receivers even in NLOS conditions or when the direct link is not sufficient. In this way, RISs provide new degrees of freedom useful to improve the network performances, as the environment is no more seen as a passive entity, but as a further support for communication needs [22].

For the reasons above discussed, a new communication model can be represented by Figure (3.6). If hypothetically every obstacles could have been coated with RISs, the behavior of the channel is fully customized after the sensing of the environment. A smart system can decide how to program the RISs in order to perform specific reflection coefficients. RISs transform the environment from a passive to an active entity overcoming the Shannon's concept of medium.

The use of MTSs as reconfigurable reflectors brings several advantages in terms of power consumption and spectral efficiency. In fact, in order to perform a stronger link in a weak communication channel, a commonly used technique is the retransmission method. With the adoption of RISs, retransmission could be no more necessary, thus bringing to an improvement of the spectral efficiency. Moreover the deployment of ad-hoc solutions, like relays, is not necessary and thus reducing the power consumption [22].

Moreover, by exploiting MTSs based solutions like RIS or IRS, it is possible to emulate the behavior of antenna arrays, with even thousands of elements, with affordable energy consumption. Unfortunately, due to technological limitations, extremely large massive antenna arrays are not of easily fabrication because of the technological limitations, as they require complex ADC chains and a high computation to drive each antenna. According with the literature, for these reasons this technology is hardly realizable, MTSs structures can be easiy fabricated because they are essentially composed by resonators with wavelength dimension and tuned with a poor number of pro-

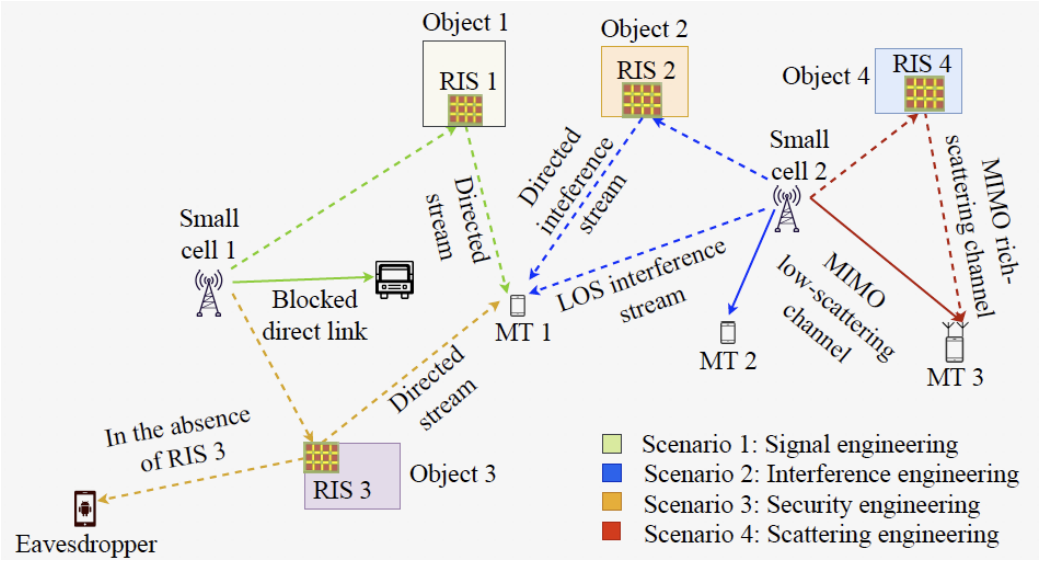

Figure 3.7: Smart Radio Environments: Example of different scenarios [22].

grammable devices like varactors and PIN diodes [22].

Nevertheless some drawbacks are present: since the environment is unknown, the RIS needs to gather and provide a huge quantity of data to the controller and this sensing effort leads to a high-energy cost because the controller will be required to process and store a huge amount of data. Hence efficient solutions needs to be developed. A possible solution could be to adopt energy harvesters to feed the controller and also, in concert with the EIT capability, MTSs can communicate each others without any backhaul physical connection.
In order to make arrangements, MTSs needs to exchange all the information they gather, with the nearby MTSs to choose the shortest path from transmitter to the receiver. The problem can be solved by using routing technology like software defined networking (SDN)) [22].

3.2.3 Software Defined Networking (SDN)

SDN [2], is a standard used in traffic engineering (TE) to manage and optimize the performance of data networks [1]. The purpose of SDN is to separate the control layer, named as Control Plane, from the forwarding layer, named as Data Forwarding Plane, in order to provide user applications to control and manage the data flow.
In modern networks, the SDN protocol is widely used and it provides the

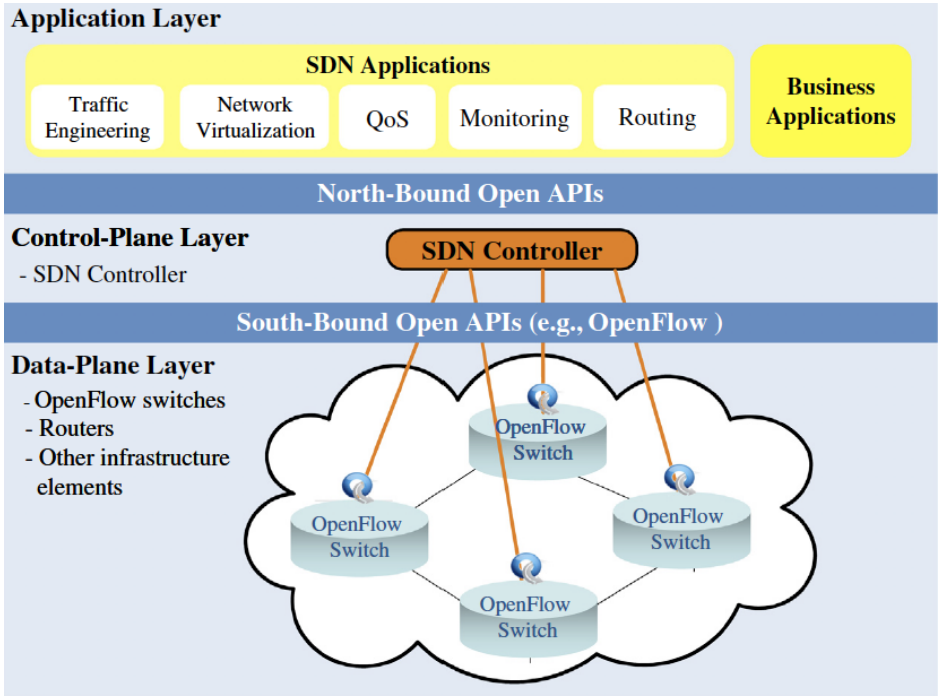

Figure 3.8: Overview on SDN Architecture [1].

presence of one or more central units named SDN Controllers, with the purpose of controlling every single switch composing the network [1].

Figure (3.8) illustrates the three layers architecture of the SDN protocol. As visible in the figure, layer interacts with the contiguous ones by means of standardized interfaces. The SDN controller, which is the intelligent part of the system, interacts directly with the routing devices and it has the management of the network, following rules imposed by the user through the application layer. The main advantages of the SDN protocol is the integration of different brand devices without any knowledge of the proprietary instructions adopted by the owner and it permits a simpler, more centralized and selective way to manage networks [1].

Thus, by hiding gateways close to the RISs, the SDN protocol can be exploited to connect RISs each others exploiting the MTS as an antenna. So several internet of things (IoT) communication protocols can be used allowing the complete integration of RIS in existing network infrastructures [16].

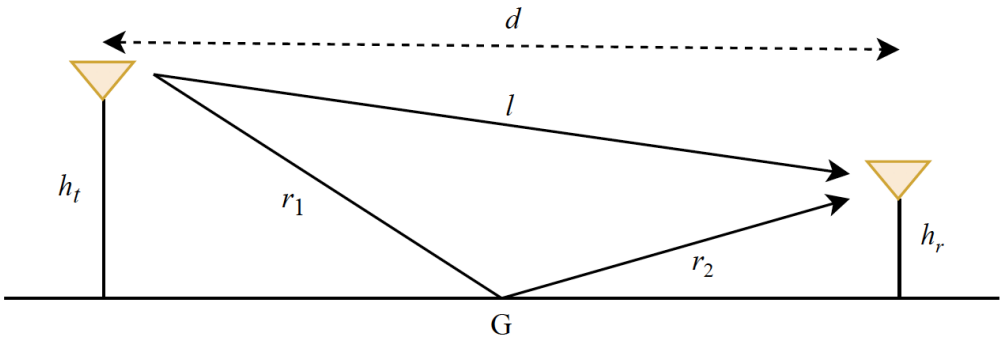

Figure 3.9: Two-rays propagation model with ground reflection [4].

3.3 Ground Reflection Scenario

To better understand the potentialities of smart radio environments throughout RISs, a simple example discussed in literature is the two-rays propagation model where an example is reported in Fig. (3.9), with one reflected path coming the ground. More specifically, three scenarios are described in the following:

- Conventional Two-Rays Model;
- MTS Two-Rays Model;
- RIS Two-Rays Model.

3.3.1 Conventional Two-Rays Model

In this model the ground is assumed to be made by homogeneous and smooth material, and to be much larger than the wavelength, so that only specular reflections are present. As an example, assuming $d \gg h_t + h_r$ and the ground reflection coefficient $\Gamma \approx -1$, according to the Fermat's Principle there is only one reflection point on the ground (G) which allows the transmitted signal to reach the receiver. In this case the power at the receiver can be described by the following Hata-like model [4]:

$$P_r \propto P_t \left(\frac{1}{d^4} \right). \tag{3.1}$$

Comparing Eq. (3.1) with Friis' Equation, the main consequence is the presence of the ground, in **LoS!** (**LoS!**) conditions at great distances, leads to a destructive effect. In fact the received power decays with the fourth power of the distance d instead of the second power [4].

3.3.2 MTS Two-Rays Model

Here the ground is considered covered by a MTS. The principal difference with the Conventional Model regards the reflection coefficient. In fact the MTS is considered able to reflect incident rays modifying the direction of the ray itself, hence Snell and Fermat Laws no more holds. Considering $R = e^{j\Delta\phi}$ where $\Delta\phi$ takes into account the angle adjustment, now it is possible to write [4]:

$$P_r \approx 4P_t \left(\frac{\lambda}{4\pi d}\right)^2. \tag{3.2}$$

By comparing Eq. (3.1) with Eq. (3.2), the received power is now scaled with $1/d^2$, and consequently is drastically increased. In fact the received power does not decay anymore with the fourth power [4].

3.3.3 RIS Two-Rays Model

Now the ground is supposed covered by a RIS made by N MTSs, each of them characterized with its own reflection coefficient Γ_i. The main advantage derives not only from the possibility to change how rays can be reflected, but also from changing the phase delay of each ray in order to perform a coherent summation at the receiver. According to this assumption and assuming $\Gamma_i = e^{j\Delta\phi_i}$, the following equation is obtained [4]:

$$P_r \approx (N+1)^2 P_t \left(\frac{\lambda}{4\pi d}\right)^2. \tag{3.3}$$

This example puts in evidence the potentialities that can be offered by RISs. In this theoretical example, the system gets the ability to enhance the received power of a quantity equal to the squared number of phases of the RIS and the received power decays with d according to the Friis' equation [4].

Chapter 4

Mathematical Models

4.1 Introduction to the problem

According to the Smart Radio Environment paradigm in order to create a connection between two points placed in a dynamic environment, the idea, as mentioned in the previous chapter, is to use RISs. Assuming the availability of SDN routing algorithms and all the sensors needed to sense the channel state information (CSI), in order to explore the potential of communication using RISs, an open problem is to derive a mathematical model capable of describing RISs and how they focus the electric field in a chosen point in the free space. In this chapter two models, numerical and analytical, are proposed using the Geometrical Optics Theory in the vicinity of the source. By seeing the RIS as an array or a matrix of antennas, the idea is to think each meta-atom composing the surface, as a spherical wave source with the possibility to tune the phase value of the electric field emitted. The scenario taken in account is the one showing the presence of a base station (BS), a mobile station (MS) and a RIS. The RIS and the BS are considered in LOS and in FF condition; the MS and the BS are in NLOS and they can not communicate. The RIS and the MS are in LOS and in NF condition but because of the absence of connection between the MS and BS, the only way to put them in communication is to exploit the RIS and its capability to shape the electric field in order to permit the connection. The goal is to characterize a specific figure of merit, the focus area (FA), able to describe somehow the quality of the system in terms of the capacity to focus most of the signal power in a specific location in which the target user is present.

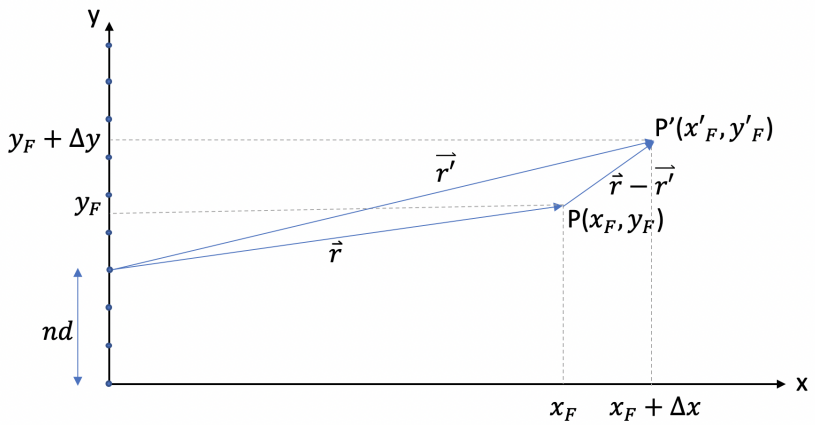

Figure 4.1: Example of a 1D-RIS

4.2 1D-RIS Numerical Model

In this section the 1D mathematical model will be discussed. To achieve this purpose, some simplifications occur:

- all the elements composing the 1D RIS must be identical
- all the elements are equidistant and spaced more than $\lambda/2$, so the mutual coupling can be neglected

RISs can be exploited to modify the phase delay in wave propagation. In the following a mathematical model is derived in order to characterize the phase delay the RIS has to impose to propagation with the purpose to focus the EM field in a specific point.
Therefore a perturbation is introduced and the system is studied.

4.2.1 Phase control

From Figure (4.1) is worth defining the following distance

$$|\vec{r}| = R = \sqrt{x_F^2 + (y_F - nd)^2} \tag{4.1}$$

where n represent the $n-th$ element in the 1D-RIS and d the distance between each element.
Each meta-atom is considered as a single spherical wave source, then it is possible to write the total electric field in the point $P(x_F, y_F)$ as

$$\vec{E}(P) = \sum_{n=0}^{N-1} C_n \vec{E_0}(\theta_n, \phi_n) \frac{e^{-j\beta R}}{R} \tag{4.2}$$

where $\vec{E_0}(\theta_n, \phi_n)$ is the electric field emitted from each meta-atom, N represents the total number of meta-atoms in the 1D-RIS and $C_n = A_n e^{j\delta_n}$ is a complex coefficient used to tailor the electric field emitted by each meta-atom, where:

- A_n is the amplitude of each element;

- δ_n is the phase delay of each element.

Substituting the above quantities and injecting Eq. (4.1) in Eq. (4.2), a new relation is obtained

$$\vec{E}(P) = \sum_{n=0}^{N-1} A_n \vec{E_0}(\theta_n, \phi_n) \frac{e^{-j(\beta\sqrt{x_F^2+(y_F-nd)^2}-\delta_n)}}{\sqrt{x_F^2+(y_F-nd)^2}} \tag{4.3}$$

where $P(x, y)$ is a generic point in the space, d is the distance between meta-atoms and n represents the n-th element. A strong simplification consists of thinking the electric field distribution $\vec{E_0}(\theta_n, \phi_n)$ as generated by a plane wave incident on the left side of the 1D-RIS. By means of this, it is possible to decompose the electric field in magnitude and phase where each element has the same electric field complex value due to the incident plane wave nature as

$$\vec{E_0}(\theta_n, \phi_n) = |\vec{E_0^n}| e^{j\psi_n} = |\vec{E_0^0}| e^{j\psi_0}.$$

The polarization of the electric field is not taken into consideration because the polarization vector is assumed perpendicular to the x/y plane.
Therefore a new equation is obtained to describe the total electric field in $P(x, y)$

$$\vec{E}(P) = \sum_{n=0}^{N-1} A_n |\vec{E_0^0}| \frac{e^{-j(\beta\sqrt{x_F^2+(y_F-nd)^2}-\delta_n-\psi_0)}}{\sqrt{x_F^2+(y_F-nd)^2}}. \tag{4.4}$$

Exploiting Eq. (4.4), it is possible to derive an expression for the single δ_n values. Those values represent the phase delay each single meta-atom must impose to the electric field, to transform the generic point $P(x_F, y_F)$ in the focus point (FP). As a matter of fact, the FP is defined as that point in the space where the single electric field contribution from the meta-atoms sums coherently.

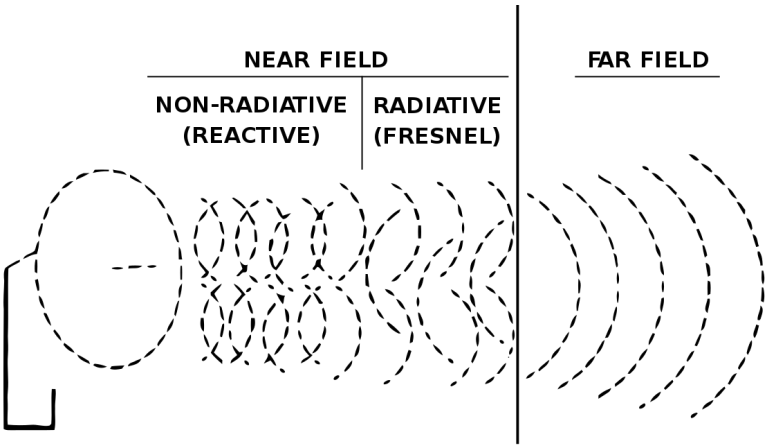

Figure 4.2: Field classification [6].

Fresnel and Fraunhofer Distances

According to literature [24], the electric field propagation in the free space comprises three different regions:

1) Non Radiative NF (Reactive)

2) Radiative NF (Fresnel Region)

3) Radiative FF (Fraunhofer Region)

The most interesting region for this application, is the Fresnel region and it is defined as the distance range from the antenna, where the electric field's phase depends strictly from the distance itself [24]. This region is particularly interesting because in the presented scenario, where a MS is left free to move into the environment close to the RIS and hence in NF.
Furthermore the electric field in the Fresnel region is radiative, hence it obeys the propagation law for a spherical wave as indicated in Eq. (4.3).
In the FF region the front wave is plane, hence the wave has constant phase and amplitude.
By means of this classification of free space, two different equations are exploited to delimit the space. Defining $D = Nd$ as the antenna dimension, or RIS dimension in this case, the following definitions are given [24]:

- Fresnel Distance (R_{FR}): It delimits the boundary between the non - Radiative NF and Radiative FF;

$$R_{FR} = \frac{D}{2}\sqrt[3]{\frac{D}{\lambda}} \tag{4.5}$$

- Fraunhofer Distance (R_{FF}): It delimits the boundary between the Radiative NF and the FF.

$$R_{FF} = \frac{2D^2}{\lambda}. \tag{4.6}$$

By means of the above definitions is possible to define a new relation between x_F, theFP, and R_{FF}, the Fraunhofer Distance, imposing that the x_F stands within the Fraunhofer distance:

$$x_F < R_{FF}.$$

Replacing in the above equation the Equation (4.6) a new fundamental relation comes out:

$$\Gamma \triangleq \frac{x_F}{2D^2}\lambda < 1 \tag{4.7}$$

where Γ is the ratio between the FP and Fraunhofer distances.

Focus Point

Recalling Eq. (4.4) by exploiting the δ_n term, the exponent of the complex exponential function can be set in such a way the EM field if focused in FP. This is obtained by setting to zero the phase term in Eq. (4.4)

$$\beta\sqrt{x_F^2 + (y_F - nd)^2} - \delta_n - \psi_0 = 0.$$

The phase value of the electric field ψ_0, can be set at any value. Therefore, for simplicity, a smart choice can be $\psi_0 = 0$, then a new equation for δ_n is obtained

$$\delta_n = \beta\left[\sqrt{x_F^2 + |y_F - nd|^2}\right]; \qquad n \in [0, N-1]. \tag{4.8}$$

The phase value in Eq. (4.8) represents the delay each meta-atom experiences. To overcome this phase delay every meta-atom composing the RIS must be tuned with a $-\delta_n$ delay and the phase delay profile represented in Fig. (4.3) is obtained. In this way a coherent field summation in FP is guaranteed.

Fig. (4.4) is obtained using Eq. (4.3). The electric field generated form the RIS is depicted, where each meta-atom is phased in order to provide the same field contribution in the FP. Then the electric field is evaluated by varying the FP along the x-wise direction. At any new FP value in the x axis, the phase distribution is evaluated.

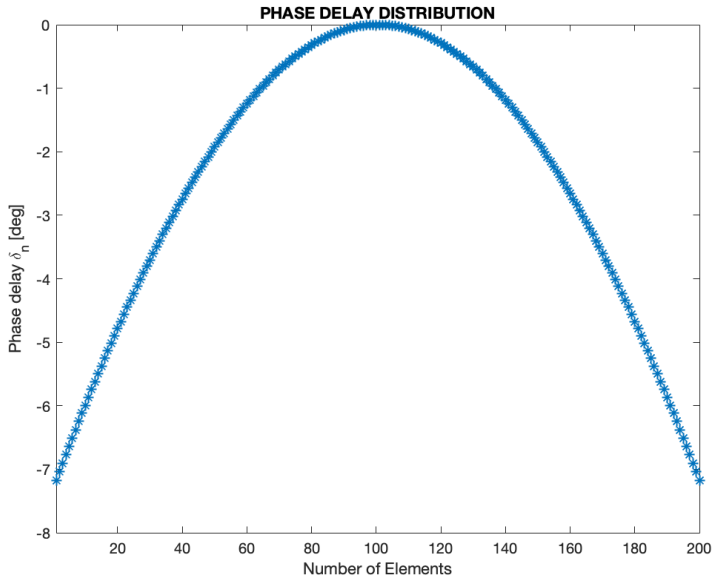

Figure 4.3: Example of phase delay evaluated for a focal point set in $x_F = D$ and $y = D/2$ which represent the middle of the metasurface $D = 1\,m$ high. ($N = 200$)

It is worth noting that the $1/x$ behavior is observed only for values $x \geq R_{FR}$ because for lower x values the near field contribution is still stronger than the far field one.

Using the same criteria, Fig. (4.5) is obtained by varying the $y_F \in [-8D; 8D]$ and fixing $x_F = D$.

4.2.2 Perturbed model

In this section the effect of a perturbation added into the FP's position is studied. The perturbed position is called $P'(x'_F, y'_F)$ where $x' = x_F + \Delta x$ and $y' = y_F + \Delta y$. This new point no longer represents the FP, so an attenuation occurs due to the phase mismatch which is the cause of an inchoerent sum. The phase delay distribution δ_n is unchanged and it has been calculated for the FP. Once the effect of a position perturbation is characterized, one can evaluate the dimension of the area around FP, named FA, outside which the electric field is significantly attenuated.

Using trigonometrical considerations from Fig. (4.1), considering the new $P'(x'_F, y'_F)$ coordinates

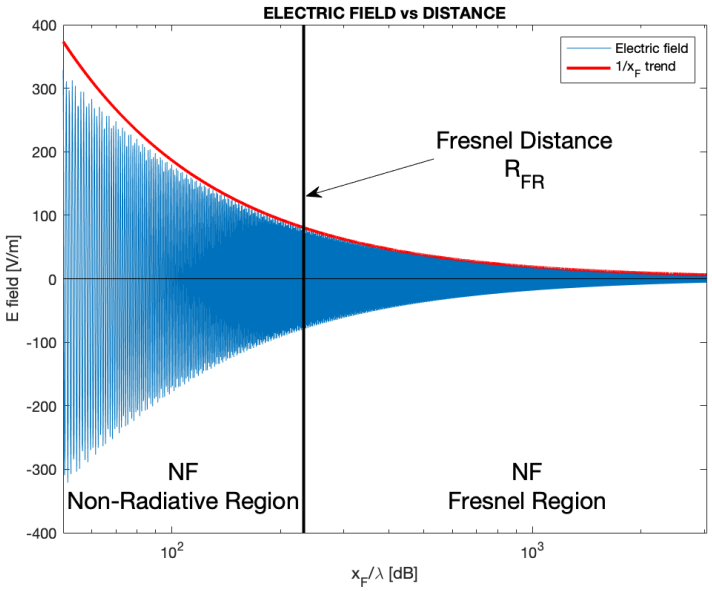

Figure 4.4: Electric field (Blue) and its theoretical trend (Red). It is shown that in the Fresnel region the electric field, varying the focal point along x, has the same $1/x$ trend of a point source in free space. The phase delay distribution was calculated for each values of x.

$$|\vec{r'}| = R' = \sqrt{(x_F + \Delta x)^2 + (y_F + \Delta y - nd)^2} \tag{4.9}$$

therefore a new equation for the electric field is obtained

$$\vec{E}(P') = \sum_{n=0}^{N-1} A_n |\vec{E_0^0}| \frac{e^{-j(\beta\sqrt{(x_F+\Delta x)^2+(y_F+\Delta y-nd)^2}-\delta_n)}}{\sqrt{(x_F + \Delta x)^2 + (y_F + \Delta y - nd)^2}} \tag{4.10}$$

then the following ratio can be defined

$$\begin{aligned} 20\log_{10}\frac{|\vec{E}(P)|}{|\vec{E}(P')|} &\leq A_{tt}^{dB} \\ &\Downarrow \\ \frac{|\vec{E}(P)|}{|\vec{E}(P')|} &\leq 10^{\frac{A_{tt}^{dB}}{20}} \triangleq \gamma \end{aligned} \tag{4.11}$$

where A_{tt}^{dB} is the maximum attenuation.

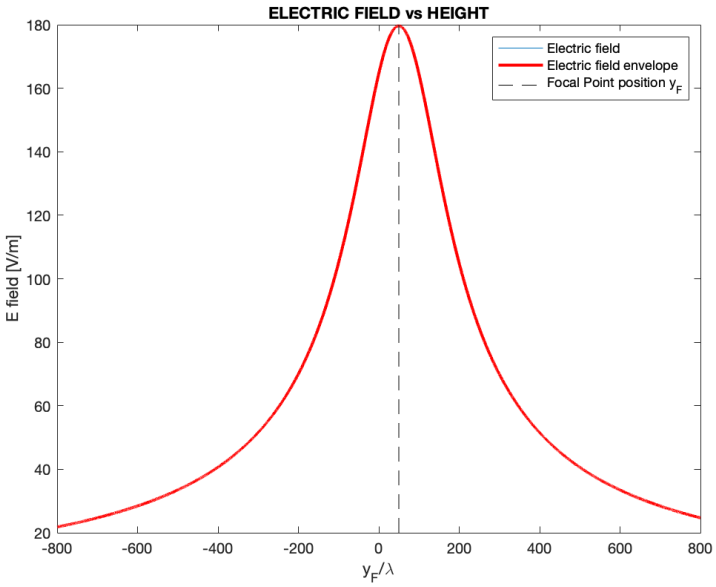

Figure 4.5: Electric field Envelope (Red). The dashed line points to the middle of the MTS.

Accordingly to [20], is useful defining as depth of focus (DoF) and width of focus (W) respectively the x and y spatial range, where the ratio between the electric field magnitude evaluated in $P(x'_F, y'_F)$ and the one evaluated in the FP, does not change more than the above attenuation γ.
The DoF and the W are obtained respectively by varying Δx from the left to the right of the x_F position and the same for Δy with y_F.
Thus an approximate expression for dimension of the FA is

$$FA = DoF \times W. \tag{4.12}$$

The DoF, or equivalently the W, is calculated fixing the other to zero. Therefore two unbound values of DoF and W were obtained despite the FA is strictly bounded to the mutual variations of these two parameters. That approximation permits to simplify the model, obtaining an overestimation of the actual FA.
In order to provide a further interpretation of the FA, this parameter denotes the ability of the RIS to focus the field. Lower FA values permit to serve more users in parallel than higher values. This consideration leads to the consequence that lower is FA, more efficiently the space will be used because in the same space more users can fit.

4.2.3 Numerical Model Results

The Figures (4.6) , (4.7) are obtained using a numerical approach to compute the FA, DoF and W. Firstly a FP is chosen and for this point the phase delay profile is calculated. Then the x and y axis are divided in equal length pieces, where for each piece the electric field is evaluated discretizing of the electric field all over the observation interval. Therefore x and y characterizations are treated separately.
In this case only x variations will be considered and a new field equation is obtained

$$\vec{E}(P') = \sum_{n=0}^{N-1} A_n |\vec{E_0^0}| \frac{e^{-j(\beta\sqrt{(x_F+\Delta x)^2+(y_F-nd)^2}-\delta_n)}}{\sqrt{(x_F+\Delta x)^2+(y_F-nd)^2}}. \tag{4.13}$$

Centering the FP x coordinate within the observation range and evaluating the electric field magnitude with Eq. (4.13), two points can be found around the FP where the electric field magnitude satisfies the attenuation limit. The distance between these points is the DoF and Fig. (4.6) gives a representation.

Similarly the W is evaluated. In this case, contrarily to the DoF case, only y variations are taken into account. Therefore a change in Eq. (4.13) is due

$$\vec{E}(P') = \sum_{n=0}^{N-1} A_n |\vec{E_0^0}| \frac{e^{-j(\beta\sqrt{(x_F)^2+(y_F+\Delta y-nd)^2}-\delta_n)}}{\sqrt{x_F^2+(y_F+\Delta y-nd)^2}}. \tag{4.14}$$

Once set the FP's y coordinate in the middle of the RIS, with the same numerical algorithm aforementioned, the two points represented in green around the FP position in Fig. (4.7) are found thus the W is obtained.

In order to obtain a characterization for the FA, several repetitions of the algorithm must be evaluated where for each running the FP is moved from close to far respect the RIS's position. By using this approach, the FP's y coordinate (y_F) is set to the middle of the RIS's height, and the x_F is left free to move.
Fig. (4.8) shows that the FA assumes higher values when FP is far from the RIS. It means that close to the RIS, small perturbations in the FP introduce a heavier phase mismatch. Meanwhile, if the FP is far away from the RIS, the phase mismatch is negligible because of the parallel-ray approximation which approximate every distance R with the distance x_F. This behavior herein observed totally agrees to the results observed in [20].

Finally in Fig. (**??**) the errors over DoF and W are shown. Since the real values of the focus parameters herein represented is unknown, the error

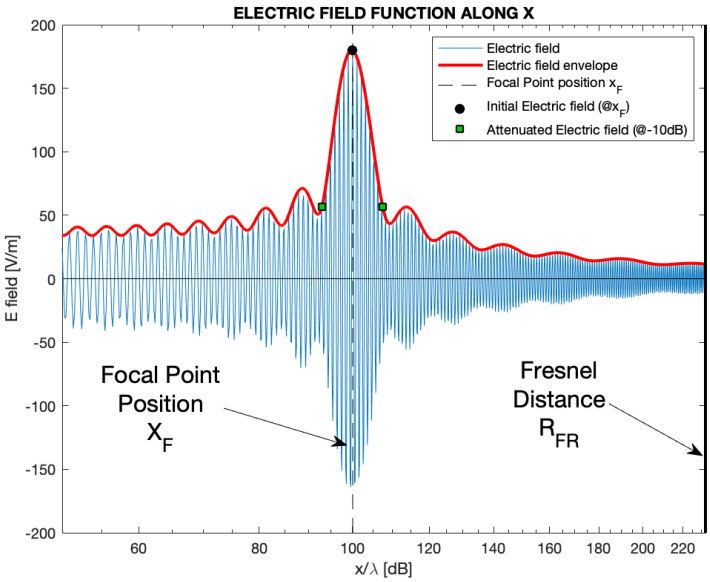

Figure 4.6: Trend of the electric field (Blue) and its envelope (Red).

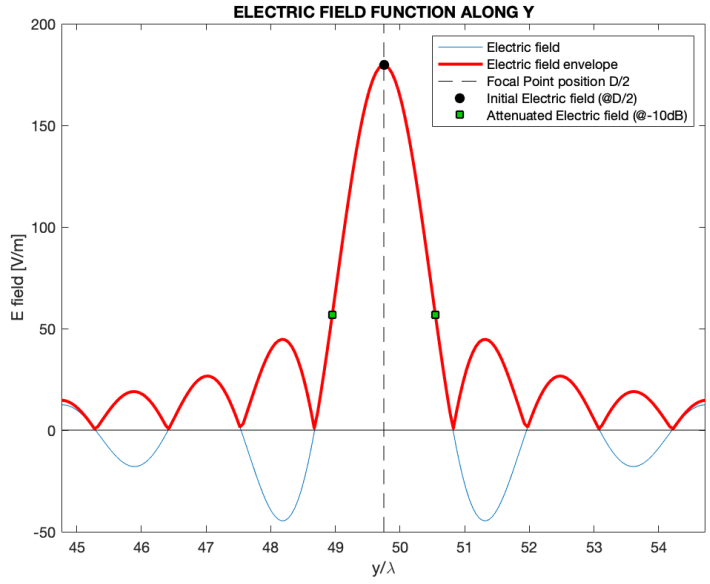

Figure 4.7: Trend of the electric field (Blue) and its envelope (Red).

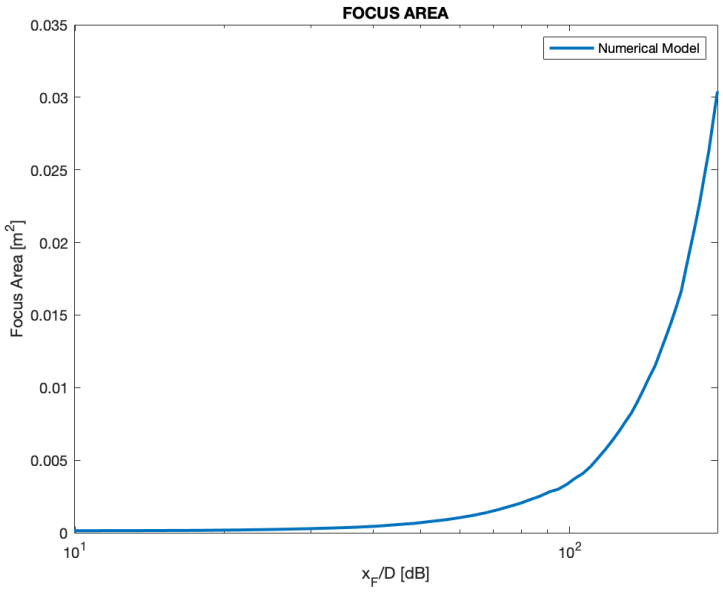

Figure 4.8: Example of the FA's trend as function of the FP position, when $y_F = D/2$.

estimation could pass through a related quantity simple to determine: the attenuation. In fact, since the DoF and the W were obtained by fixing the maximum attenuation value permitted by the system, the idea is to reintroduce these values in the field equations (4.13) , (4.14) and verify if the bound over the attenuation was respected. The deviation from these values is the error.

Observing the Figures (4.9) , (4.10) is easy to see that closer to the RIS the algorithm is more inaccurate. This behavior is due to the discretization step everywhere constant, in fact the FA is small closer the RIS and big farther, hence the error introduced for values closer the RIS produces this behavior.
In the following an extension of the 1D-RIS model is presented. The goal is to extend the numerical algorithm to a 2D-RIS in order to study the electric field when the RIS is an entire surface.

4.3 2D-RIS Numerical Model

In this section will be discussed the mathematical model for the 2D-RIS. In this case the 2D representation is an extension of the work made for the 1D model, hence all the 1D assumptions are valid. Moreover, to characterize

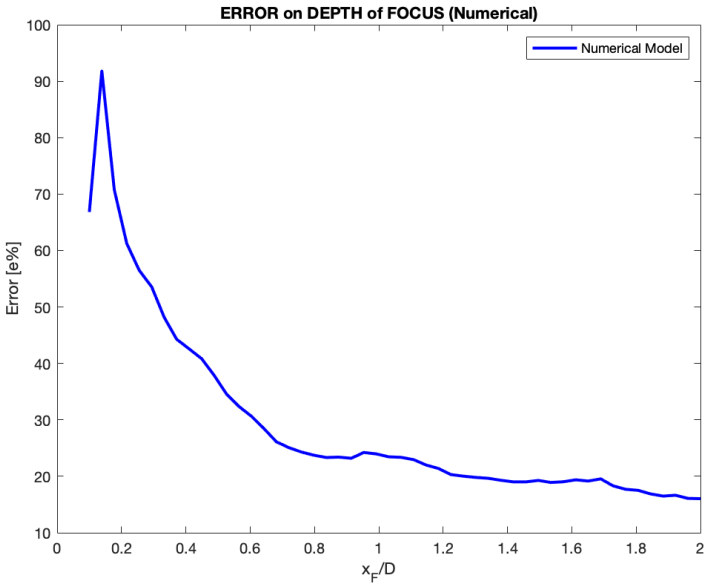

Figure 4.9: DoF's error for the numerical algorithm.

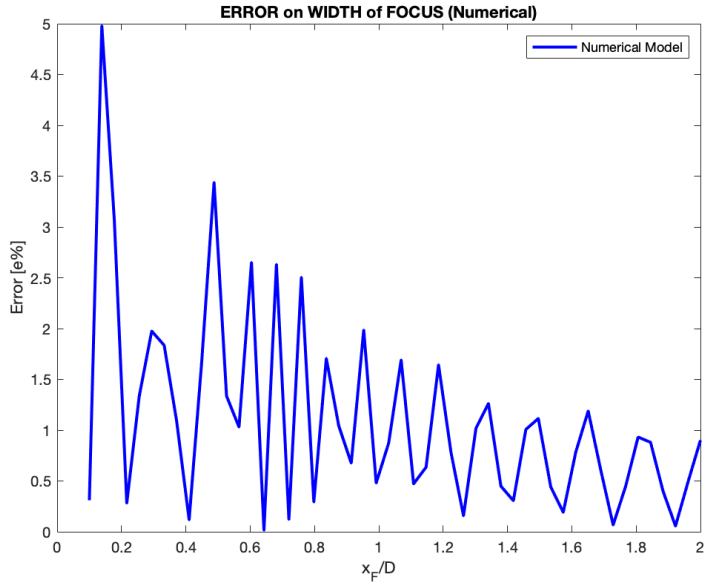

Figure 4.10: W's error for the numerical algorithm.

DoF, W and hence the FA, the same numerical algorithm described in the 1D model is used. The idea is to adapt the algorithm in order to exploits also the z coordinate in the focusing.

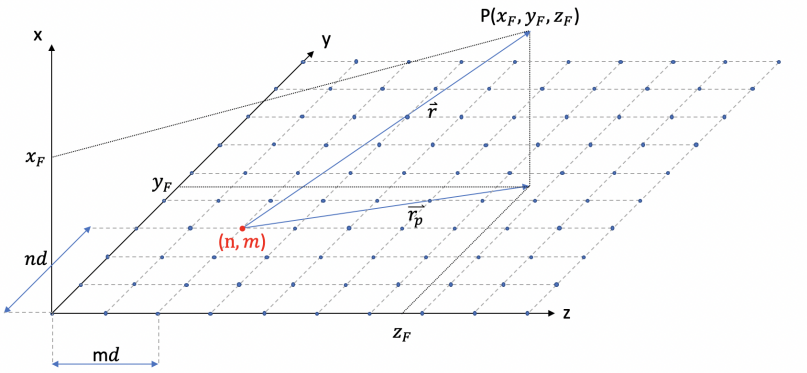

Figure 4.11: Example of a 2D-RIS

4.3.1 Phase Control

As for the 1D Model, from Fig. (4.11) the distances vector $\vec{r}$ in the three dimensional space is defined by the following relation

$$|\vec{r}| = R = \sqrt{x_F^2 + (y_F - nd)^2 + (z_F - md)^2} \tag{4.15}$$

then the total electric field in $P(x_F, y_F, z_F)$ is represented by

$$\vec{E}(P) = \sum_{n=0}^{N-1} \sum_{m=0}^{M-1} A_n |\vec{E_0^0}| \frac{e^{-j(\beta\sqrt{x_F^2+(y_F-nd)^2+(z_F-md)^2} - \delta_{n,m} - \psi_0)}}{\sqrt{x_F^2 + (y_F - nd)^2 + (z_F - md)^2}}. \tag{4.16}$$

Fig. (4.12) represents the phase delay distribution by which the Fig. (4.13) is obtained. The RIS used has dimensions $D_y \times D_z$ where $D_y = d(N-1)$ and $D_z = d(M-1)$.
The 3D phase delay distribution $\delta_{n,m}$ in Eq. (4.17) is obtained from Eq. (4.16). As in the previous section, the exponent in the exponential function is forced arbitrarily to zero. Accordingly to that, the distance R is no more significative in Eq. (4.16) and the electric field summation is coherent into the FP. Thus Fig. (4.13) is obtained.

$$\delta_{n,m} = \beta \left[\sqrt{x_F^2 + (y_F - nd)^2 + (z_F - md)^2} \right]; \quad n, m \in [0, (N-1) \times (M-1)]. \tag{4.17}$$

A remarkable result shown in Fig. (4.13) is the field profile for $x_F > R_{FR}$ still have a $1/x_F$ behavior as seen in the 1D Model. This means that the RIS

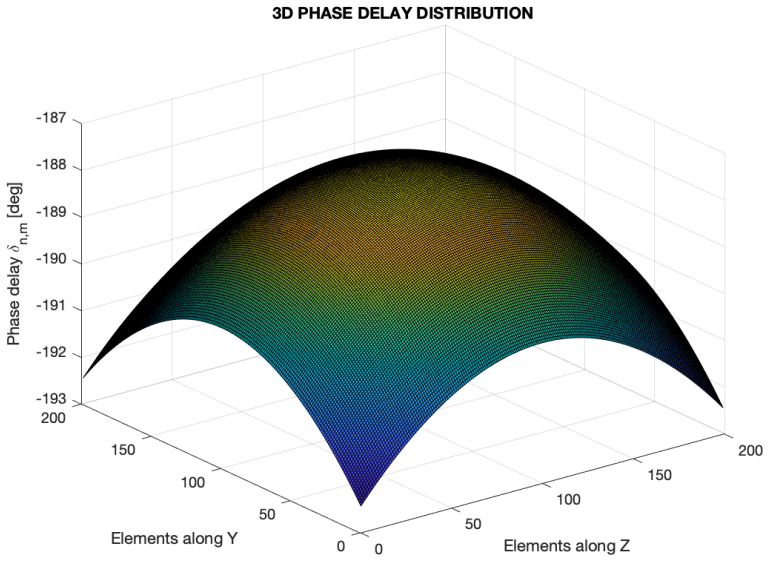

Figure 4.12: Example of phase delay evaluated for a FP set in $x_F = D_y$, $y = D_y/2$ and $z = D_z/2$ where RIS a square surface with area 1 m^2.

is acting like a point source, hence the electric field registered in the FP has no dependency by the phase mismatch between meta-atoms.
It worth saying for the sake of simplification in the 3D calculation, the electric field polarization is not taken in account. The effect of polarization is in general not negligible, but imaging at the receiver an antenna capable to recognize the polarization of the EM wave, is possible to assume the polarization match between the electric field and the receiving antenna feasible.

In this section the 3D model is introduced and it is used to evaluate the electric field in the FP. In the following a perturbation is introduced with the aim of evaluate the perturbation parameters DoF, W and FA also in the 3D model.

4.3.2 Perturbed Model

Herein the electric field variation along the three dimensions is studied. Also in this case, the goal is to characterize the FA.
Similarly as done in 1D model, an equation for each degree of freedom must be written treating each case independently between each others. Firstly an equation for the DoF is obtained

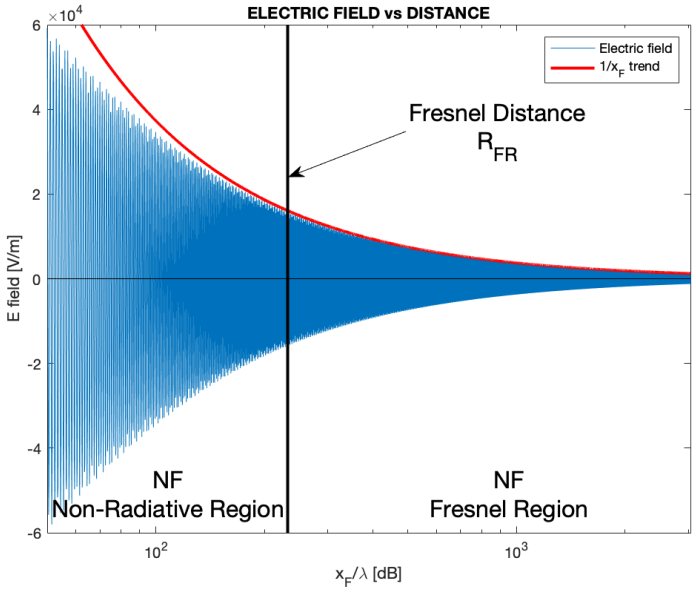

Figure 4.13: Electric field (Blue) and its theoretical trend (Red).

$$\vec{E}(P') = \sum_{n=0}^{N-1} A_n |\vec{E_0^0}| \frac{e^{-j(\beta\sqrt{(x_F+\Delta x)^2+(y_F-nd)^2+(z_F-md)^2}-\delta_{n,m})}}{\sqrt{(x_F+\Delta x)^2+(y_F-nd)^2+(z_F-md)^2}}; \tag{4.18}$$

then, adopting similar considerations, an equation for the W along the y axis is derived

$$\vec{E}(P') = \sum_{n=0}^{N-1} A_n |\vec{E_0^0}| \frac{e^{-j(\beta\sqrt{x_F^2+(y_F+\Delta y-nd)^2+(z_F-md)^2}-\delta_{n,m})}}{\sqrt{x_F^2+(y_F+\Delta y-nd)^2+(z_F-md)^2}}; \tag{4.19}$$

finally an equation for the W along z axis is

$$\vec{E}(P') = \sum_{n=0}^{N-1} A_n |\vec{E_0^0}| \frac{e^{-j(\beta\sqrt{x_F^2+(y_F-nd)^2+(z_F+\Delta z-md)^2}-\delta_{n,m})}}{\sqrt{x_F^2+(y_F-nd)^2+(z_F+\Delta z-md)^2}}. \tag{4.20}$$

Exploiting the Equations (4.18) , (4.19) , (4.20), and dividing the x/y plane in equal pieces, the same algorithm described in the 1D-RIS model can be adopted to obtain the three focus parameters along x, y and z. Solving

the field equations recursively, a Focus Volume (FV) is determined within it the attenuation is always lower than a fixed value. Nonetheless, in this work the FV is not investigate, because the scenario examined considers the z coordinate in the FP unchanged, or at least it changes very slowly compared to x/y coordinates. Therefore, the parameter considered is the FA and it is characterized as a function of the entire x/y plane.

In the past section the mathematical description and the numerical algorithm used to evaluate the 2D-RIS model are described. In the following section the results obtained from simulations are highlighted.

4.3.3 Numerical Model Results

Similarly as seen in the 1D-RIS model, Figures (4.14) , (4.15) show the electric field as a function of the focus parameters. The main difference between the 1D Model and the 2D model is in the electric field values. Indeed, increasing the dimension of RIS by adopting an addition degree of freedom along the z axis, the ability to focus the electric field in the FP improves. The visible consequence in the FP is the electric field intensity is higher than in the 1D Model, and the peak becomes narrower. It drives to the consequence that for slight displacement from the FP, the magnitude of the electric field decrease faster. This behavior is remarkable for applications because it describes an enhancing in the RIS's focusing ability.

Figures (4.16) , (4.17) show the difference between the £D electric field in NF and in FF conditions. It is worth noting when the FP is near the RIS, the system has the possibility to discriminate the position because the peak is narrow and well defined. On the contrary when the RIS focuses the field in the FF, it loses the ability to discriminate the position and it can only discriminate in angles exactly as antenna arrays do. In Fig. (4.17) is also represented a plane which cuts lengthwise the beam. It represents the Threshold Electric field (E_{th}) used to estimate the FA. This representation highlights the aforementioned RIS's behavior in the FF.

In order to calculate the FA also in the 2D-RIS Model all the x/y plane must be taken into consideration. Each value of area was evaluated fixing several FPs in the x/y plane with a constant value of z and making vary the x/y coordinates in the vicinity of the FPs without change the phase delay distribution. Also in this case the x/y plane was discretized and for each FP, the FA was numerically calculated.

Fig. (4.18) represents the 3D graph of the FA. The minimum FA value is placed at $x_F \simeq D_x$ and $y_F \simeq D_y/2$. This point represent the FP where the RIS can focus the electric field as best as its possibility. It is shown that

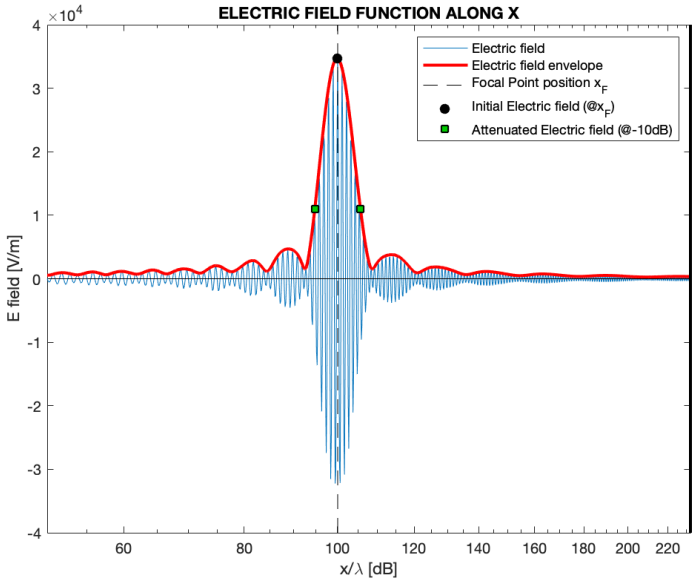

Figure 4.14: Depth of Focus

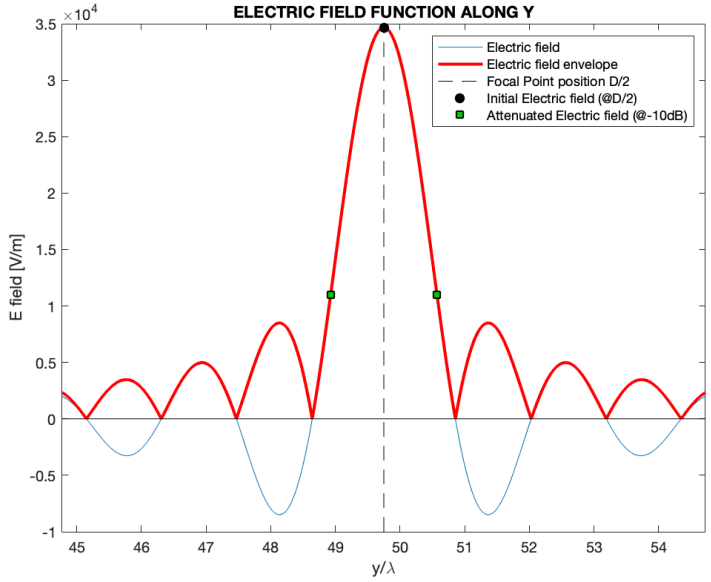

Figure 4.15: Width of focus (y)

the minimum FA value is reached when the distance from the RIS is equal to its size. This is a remarkable consequence to use for the dimensioning of the system.

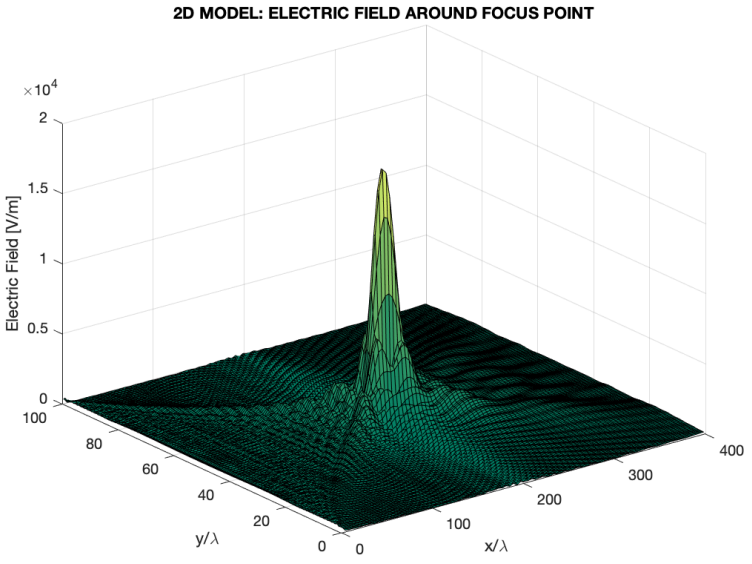

Figure 4.16: Focusing ability in NF condition

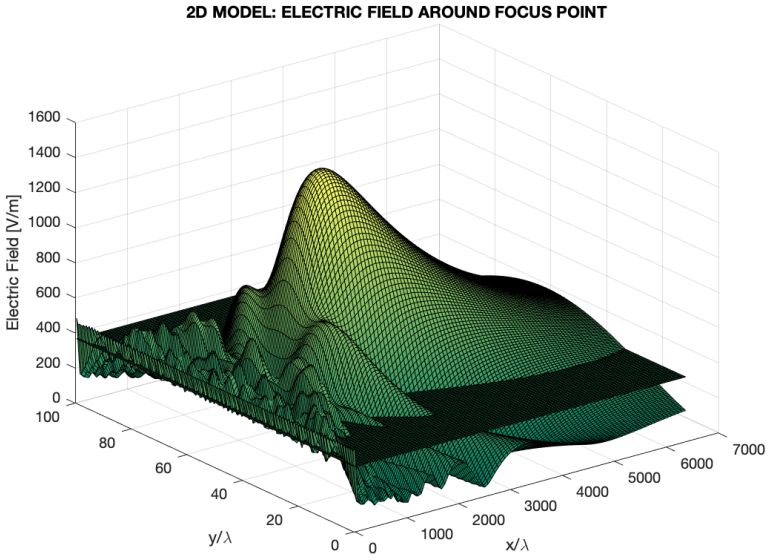

Figure 4.17: Focusing ability in FF condition.

In this section, a mathematical model for the 2D-RIS is obtained and the main results deriving from the simulations are described. In the following a new approach is studied with the aim to obtain an analytical mathematical

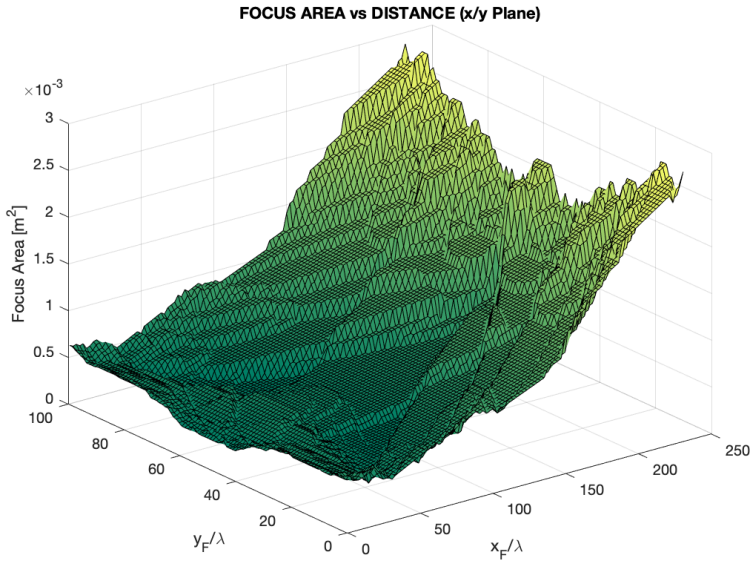

Figure 4.18: Trend of the FA as a function of the FP position. $x_F \in [0, R_{FR}]$ and $y_F \in [0, D_y]$.

description of the focus parameters in order to simplify the computational effort required to their estimation.

4.4 1D-RIS Analytical Model

Starting from the equations obtained for the 1D model, the purpose is to describe analytically the system in order to find a faster model for the FA calculation passing through the estimation of DoF and W. For the sake of simplicity, only the 1D-RIS model is taken in account, but the following considerations can be extended to the 2D-RIS model.

4.4.1 Mathematical description

The same assumptions made in the previous sections are made, thus Equations (4.1) and (4.4) are modified assuming $\psi_0 = 0$, $|\vec{E}_0^0| = costant$, $A_n = 1$ and $\delta_n = \beta R$, hence the following expression is obtained

$$R = \sqrt{x_F^2 + (y_F - nd)^2}$$
$$\vec{E}(P) = |\vec{E_0^0}| \sum_{n=0}^{N-1} \frac{1}{R} \tag{4.21}$$

then replacing x_F, y_F with $x'_F = x_F + \Delta x$ and $y'_F = y_F + \Delta y$ respectively, new equations for the perturbed point $P'(x'_F, y'_F)$ are obtained

$$R' = \sqrt{(x_F + \Delta x)^2 + (y_F + \Delta y - nd)^2}$$
$$\vec{E}(P') = |\vec{E_0^0}| \sum_{n=0}^{N-1} \frac{e^{-j\beta(R'-R)}}{R'}. \tag{4.22}$$

Depth of Focus

In order to get an expression for a DoF, some more assumptions are needed. The first hypothesis is to left as free to move only one variable at time. For this reason Δy is set to zero and then some mathematical manipulations on R' are necessary

$$\begin{aligned} R' &= \sqrt{(x_F + \Delta x)^2 + (y_F - nd)^2} = \\ &= \sqrt{x_F^2 + \Delta x^2 + 2x\Delta x + (y_F - nd)^2} = \\ &= \sqrt{R^2 + \xi} \end{aligned}$$

assuming $\xi = \Delta x^2 + 2x\Delta x$ and putting in evidence R^2 inside the square root, the following is obtained

$$R' = R\sqrt{1 + \xi/R^2}.$$

The second hypothesis is set $\xi << R$ so the above expression is expressed using the second order Taylor series expansion

$$R' \simeq R\left(1 + \frac{\xi}{2R^2}\right).$$

The third hypothesis is $R' \simeq R$ as a consequence of the parallel-ray approximation, thus another electric field expression is

$$\vec{E}(P') \simeq |\vec{E_0^0}| \sum_{n=0}^{N-1} \frac{e^{-j\beta(R'-R)}}{R}$$
$$R' - R \simeq \frac{\xi}{2R} = \frac{\Delta x^2}{2R} + \frac{x\Delta x}{R} \simeq \frac{x}{R}\Delta x = \frac{\Delta x}{\sqrt{1 + \frac{(y_F - nd)^2}{x_F^2}}}.$$

Finally the expression for $R' - R$ can be injected and a new expression for the perturbed electric field is obtained

$$\vec{E}(P') \simeq |\vec{E_0^0}| \sum_{n=0}^{N-1} \frac{e^{-j2\pi f_n \Delta x}}{R} \tag{4.23}$$

where f_n is defined as Spatial Oscillating Frequency because it covers the role of frequency interpreting the Eq. (4.23) as a sum of phasors. It is worth noting it depends by the ratio between the height of the RIS and the distance of the FP from the the RIS itself as it is shown in the following

$$f_n = \frac{1}{\lambda\sqrt{1 + \frac{(y_F - nd)^2}{x_F^2}}}. \tag{4.24}$$

Equations (4.21) , (4.23) can be injected in Eq. (4.11), then a new relation can be written as

$$\left| \sum_{n=0}^{N-1} \frac{e^{-j2\pi f_n \Delta x}}{R} \right| - \gamma \left| \sum_{n=0}^{N-1} \frac{1}{R} \right| = 0$$

where the second addend is a known constant named Threshold Electric Field (E_{th}) and the equation is non-linear in Δx. Thus the following is obtained

$$\left| \sum_{n=0}^{N-1} \frac{e^{-j2\pi f_n \Delta x}}{R} \right| - E_{th} = 0. \tag{4.25}$$

For symmetrical reasons highlighted in Fig. (4.19), the DoF is set $DoF = 2\Delta x$ where Δx is obtained from Eq. (4.25) by means of non-linear solving methods.

Width of Focus

The W is evaluated with the same hypothesis made for the DoF, except for one: in this case Δy is left free to move and Δx is set to zero. Thorough the same passages made before, the following equation is obtained

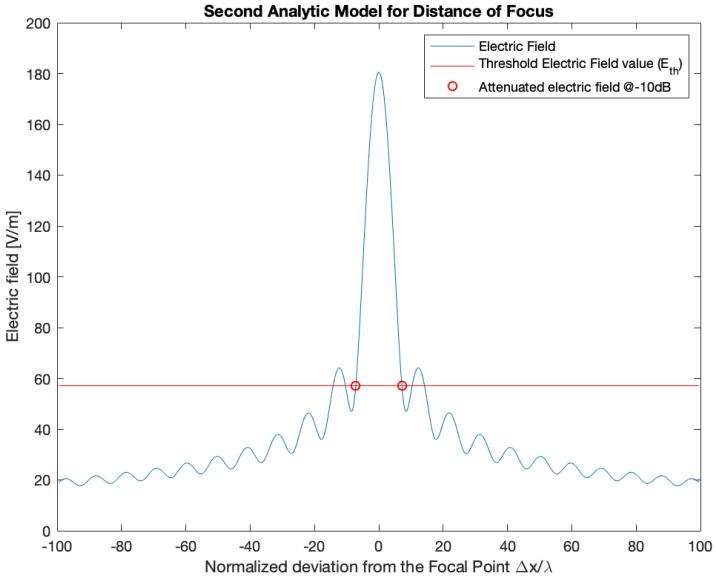

Figure 4.19: Electric field along x axis with in red the threshold value E_th.

$$\vec{E}(P') \simeq |\vec{E_0^0}| \sum_{n=0}^{N-1} \frac{e^{-j2\pi f_n \frac{(y-nd)}{x}\Delta y}}{R} \tag{4.26}$$

and then the final equation for the W looks similar to Eq. (4.25)

$$\left| \sum_{n=0}^{N-1} \frac{e^{-j2\pi f_n \frac{(y-nd)}{x}\Delta y}}{R} \right| - E_{th} = 0 \tag{4.27}$$

As for the DoF calculation, for symmetry reasons highlighted in Fig. (4.20), the W is set $W = 2\Delta y$ where Δy is obtained from Eq. (4.27) by means of non-linear solving methods.

Figures (4.19) , (4.20) show the variability of the electric field for several displacement points represented by Δx and Δy along x and y axis respectively. These figures are a representation of Equations (4.25) , (4.27) where the ambition is to show how the electric field varies. The intersection points are the solutions of the equations and they define the DoF and the W. As visible in the figures, the maximum peak obtained for $\Delta x = \Delta y = 0$ denotes the FP's position.

In the following the main features that characterize the RIS's analytical model are discussed.

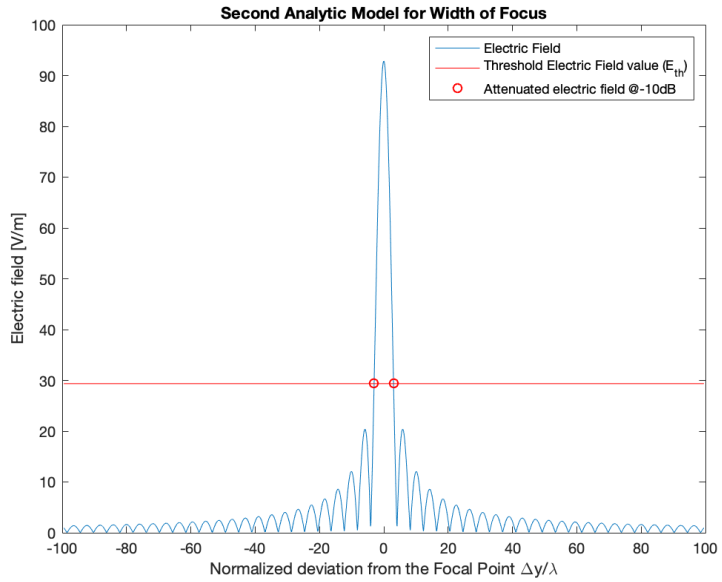

Figure 4.20: Electric field along y axis with in red the threshold value E_th.

4.4.2 Analitycal Model Results

Figures (4.21) , (4.22) , (4.23) represent the focus parameters. As shown in Fig. (4.23) the trend of the FA is the same shown in Fig. (4.8) even if, for some reasons related to the precision of the algorithms, the two curves refers to the slightly different area values.

Similarly as done for the numerical method, the error has been evaluated indirectly through the definition of the attenuation. As depicted in Figures (4.24) , (4.25) this method shows good performances in FA calculation because the error remains confined under low values. The principal drawback put in evidence from Fig. (4.24) is that meanwhile the error on the W saturates, the error on DoF grows linearly. Nevertheless, because the anlytical model is obtained for evaluate the FA in the vicinity of the RIS, the growth of DoF error is limited by the model itself. Moreover Fig. (4.25) shows an initial oscillation in the error. This issue is also visible in Fig. (4.22) and it is due to the approximation used in the model. In fact in the mathematical steps described in the previous section, it is assumed $x_F \gg (y_F - nd)$, hence for values of x_F near zero this condition is no longer true.

In this section the analytical model is introduced and characterized. In the following a comparison between numerical and analytical algorithm has been provided, in order to highlights the main features of the algorithms.

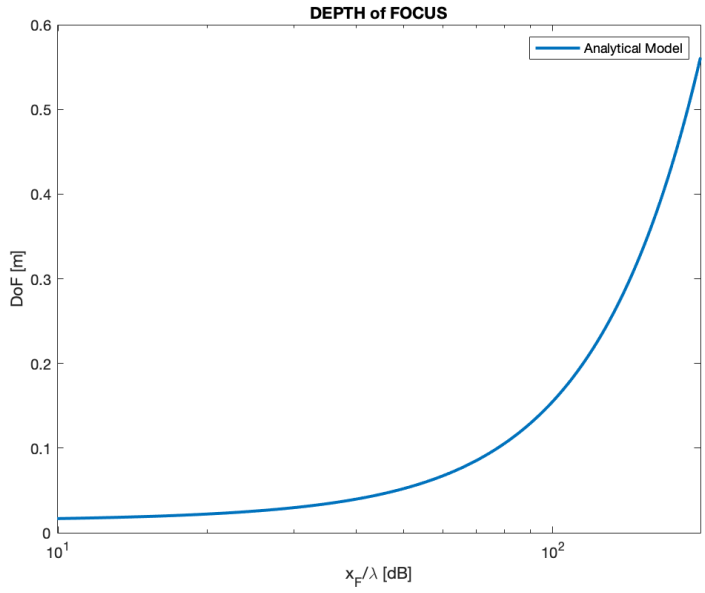

Figure 4.21: DoF analytically evaluated.

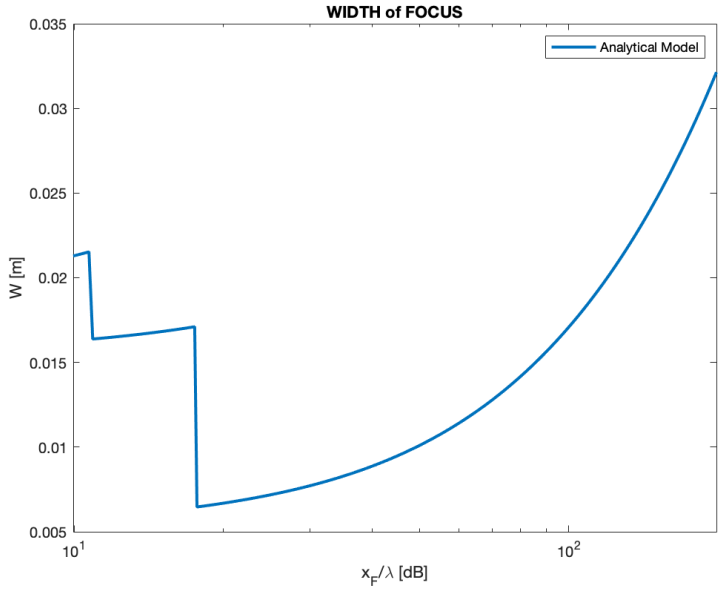

Figure 4.22: W analytically evaluated.

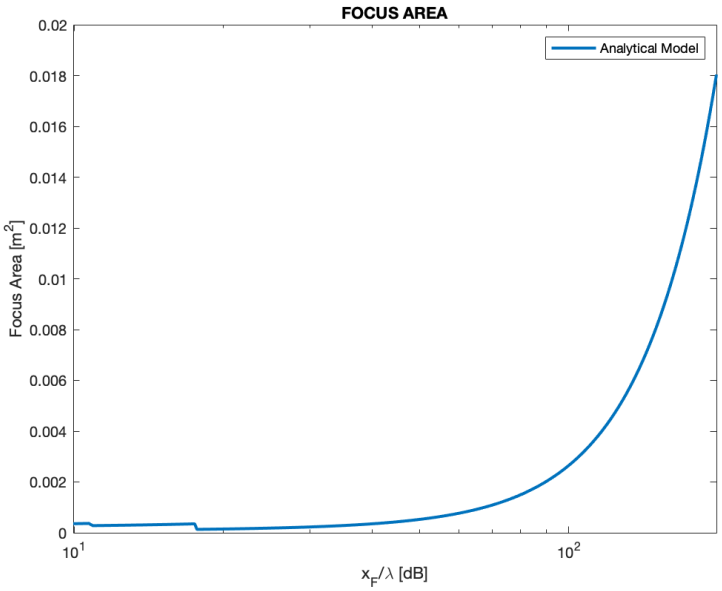

Figure 4.23: FA analytically evaluated.

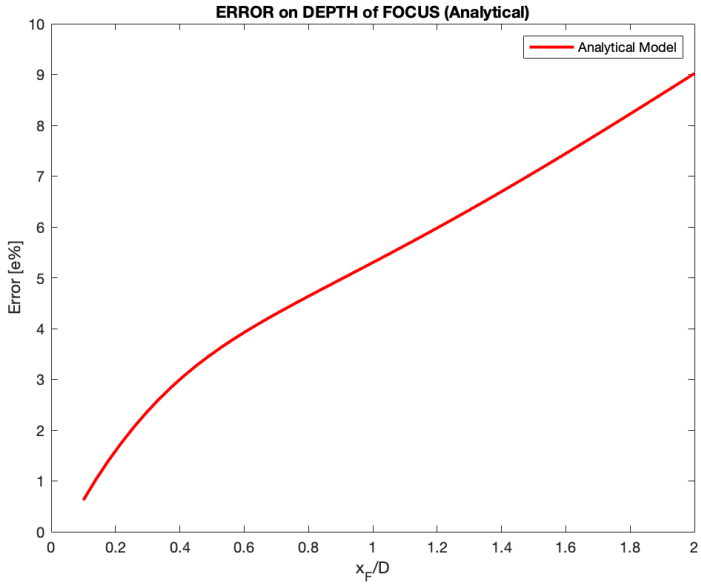

Figure 4.24: DoF's error on the analytical algorithm.

4.5 Numerical vs Analyical: Models Comparison

In the previous sections numerical and analytical models are described and each of them leads to the FA calculation. In order to understand the dif-

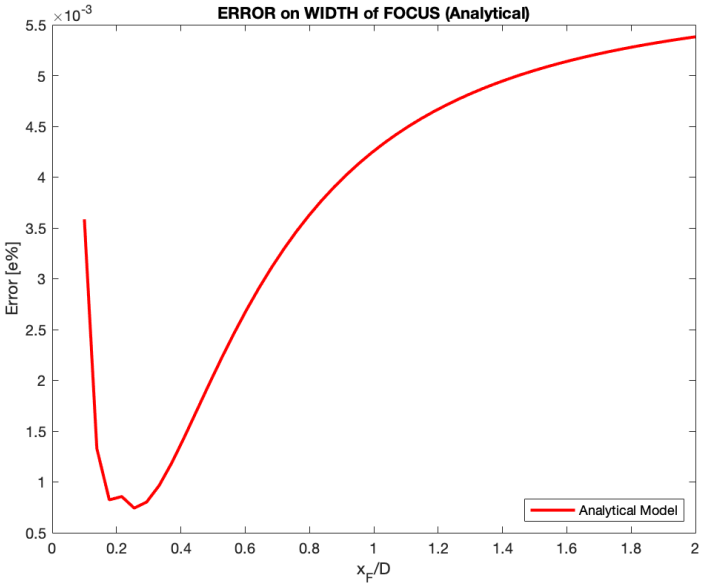

Figure 4.25: W's error on the analytical algorithm.

ferences between models, errors are taken into account and compared. For comparison reasons, the 1D-RIS numerical model is confronted with the 1D-RIS analitycal model. The 2D-RIS numerical model is not taken into consideration, but similar consequence can be extended to this model. In fact the 1D Model is a particular application of the 2D model.

4.5.1 Depth of Focus

Fig. (4.26) compares the DoF's error between Analytical and Numerical algorithms. The results obtained from the two algorithms demonstrate that for higher distances represented by x_F, the errors on numerical and analytical algorithms come closer. On the contrary for lower distances, errors are distant from each other. The error is evaluated by means of the field equation, since the DoF is defined as the maximum deviation from the FP where the electric field attenuation is kept lower than a fixed value, the value obtained by the algorithm is feed-backed to the electric field equation and the mismatch between the theoretical and real attenuation is evaluated and represented in figure.
The numerical error, represented in blue, assumes an hyperbolic behavior along the x axis, and this is due to the piecewise method used to evaluate the electric field. As a matter of fact, the discretization step used is the same

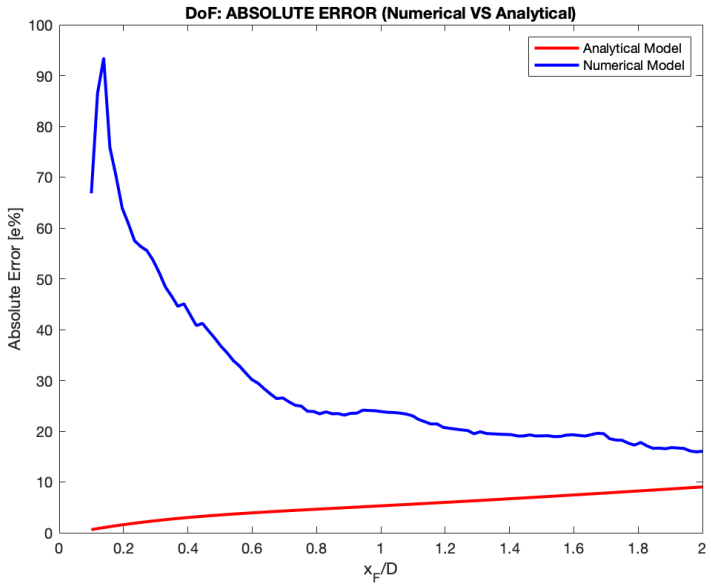

Figure 4.26: DoF, error comparison between numerical and analytical.

all over the x axis, hence it is more significant for values closer to the RIS where the DoF is lower. On the contrary, analytical errors are lower closer the RIS. Observing this behavior, it emerges that for lower values of x_F the analytical method offers better performances than the numerical one. As a matter of fact, the choice between numerical must be taken in function of the distance to be investigated.

4.5.2 Width of Focus

Fig. (4.27) compares the W's error between analytical and numerical. Similarly as done for DoF, also the W's error is evaluated using the attenuation. The numerical error represented in blue, has an oscillating behavior due to the electric field nature and its envelope can be approximated by an hyperbolic function depending on the distance. As seen for the DoF's error, the piecewise algorithm used in the numerical method introduces higher errors closer to the RIS. On the contrary, the analytical error demonstrates to be very accurate also closer the RIS and with values slightly above zero.

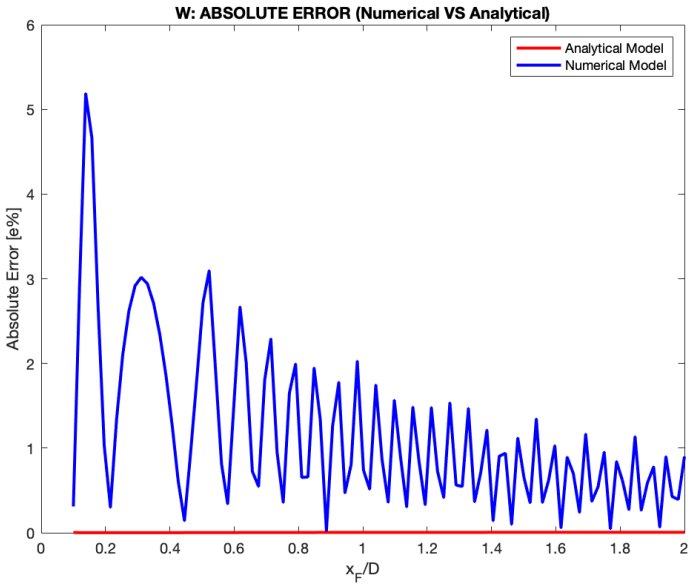

Figure 4.27: W, error comparison between numerical and analytical methods.

4.5.3 Focus Area

The error over the FA is impossible to determine because the same method used for DoF and W can not be use. As a matter of fact, the errors for DoF and W are estimated basing on the attenuation. For this reason is impossible to infer the real error on the perturbation parameters. Especially for the FA, which represent an upper bound of the real FA. In order to provide a qualitative description of the error on the FA, a mathematical formulation is investigated.
Defining $\widehat{DoF} = DoF + \Delta e_{DoF}$ and $\widehat{W} = W + \Delta e_W$ where the Δe represent the real error on DoF and W, by using the FA definition the following is obtained

$$\begin{aligned}\widehat{FA} = \widehat{DoF} \times \widehat{W} = (DoF + \Delta e_{DoF})(W + \Delta e_W) = \\ = DoF \times W + DoF\Delta e_W + W\Delta e_{DoF} + \Delta e_{DoF}\Delta e_W = \\ = FA + DoF\Delta e_W + W\Delta e_{DoF} + \Delta e_{DoF}\Delta e_W\end{aligned}$$

neglecting the product $\Delta e_{DoF}\Delta e_W$ because it is assumed near zero, the error can be defined by the following

$$\Delta e_{FA} \simeq DoF\Delta e_W + W\Delta e_{DoF}. \tag{4.28}$$

Eq. (4.28) shows that the FA error not depends exclusively from errors on DoF and W, but also from the parameters themselves. As a matter of fact, in order to provide an accurate estimation for the FA, the model used to obtain the DoF and the W must be accurate.

In this chapter the main algorithms have been described highlighting the characteristics of each one. In the next chapter, using the models just studied, some applications of interest will be presented.

Chapter 5

RIS's Applications Examples

5.1 Focus Area Interpretation

All mathematical models described so far now, have the final purpose to give a 2D or 3D representation of the FA. The FA shows the ability of the RIS to realize reliable connections and it is a function of the distance.
A physical interpretation of the FA is the area within a device, placed in the FP, will be connected to the RIS independently by the presence of the other devices provided that they are outside of the FA. It leads to the consideration that by means of RISs some independent paths can be created and orthogonal channels between the RIS and the receiving devices can be set up. The absence of interference is guaranteed electromagnetically, hence the environment no longer represent a passive obstacle, but by means of MTMs the environment acts accordingly to our needs.

As a matter of fact, a new mathematical entity can be defined with the purpose of describing the number of independent paths or connections per square meters and it is referred to as orthogonal links density function (OLDF).

5.1.1 Orthogonal Links Density Function (OLDF)

As mentioned above, the OLDF describes the density of orthogonal paths between the RIS and the receiving devices. It is strongly related to the FA by means of the following relationship

$$\mathcal{A}(x, y) = \frac{1}{FA(x, y)} \tag{5.1}$$

where the FA is a function of the x/y coordinates because, as aforementioned, it is obtained varying the FP position in the x/y plane. Eq. (5.1) represents

the density of orthogonal connections per area unit, hence the number of connections C can be represented by the following equation

$$C = \iint_{\Sigma} \mathcal{A}(x, y) dx dy \tag{5.2}$$

where Σ represents the observation area.
In order to understand the possible implications derived by using RISs, in the following an industrial scenario has been proposed.

5.1.2 Example: Industrial IoT (IIoT)

Industrial Internet of Things (IIoT) is the IoT for industrial sector. The evolution of the technology leads us to a new industrial revolution called Industry 4.0. The increasing number of sensors in automated machines and the massive enhancing of data rates will drive the next step in the technological process towards a system architecture with low latency and able to support all traffic generated from an high density of sensors [13].

MTMs can be used to provide additional interesting functionalities in IoT scenarios and in order to provide an example, an operative case will be presented. The scenario considered is an industrial building 5 m high and 15 m long wherein a 15 m long product chain is working and a RIS is installed on the ceiling in the middle of the building's length. The machinery installed is supplied by an high number of sensors and devices which have to communicate with a cloud system in order to collect data. The purpose is to understand how many sensors can communicate simultaneously with the RIS without the need to consider MAC protocols which could require some overhead as well as random delay due to retransmissions.
In order to simplify the problem, the technological limits due to programming the RIS and to implement orthogonal channels with the sensors, is not considered in this scenario.

Firstly the RIS's size has to be chosen. RISs perform the best when the FP's distance from the center is the same of the RIS's dimension. Therefore, since the height of the building is $5\,m$, the chosen RIS's size is $(5 \times 5)\,m$. Fig. (5.1) shows the FA as function of x/D where D is the RIS's size. When $x = 5\,m$ the FA $\simeq 150\,cm^2$ as indicated in figure, thus choosing a device area lower than the FA's value it is guaranteed that for each orthogonal path there is only a single device.
Secondly, according to the above considerations, a device area of $100\,cm^2$ has been chosen which describes a squared area device with side $l = 10\,cm$.

Finally the OLDF is obtained from simulations and it is represented in Fig. (5.2). It shows that within the range from 5 to $10\,m$, the links density is

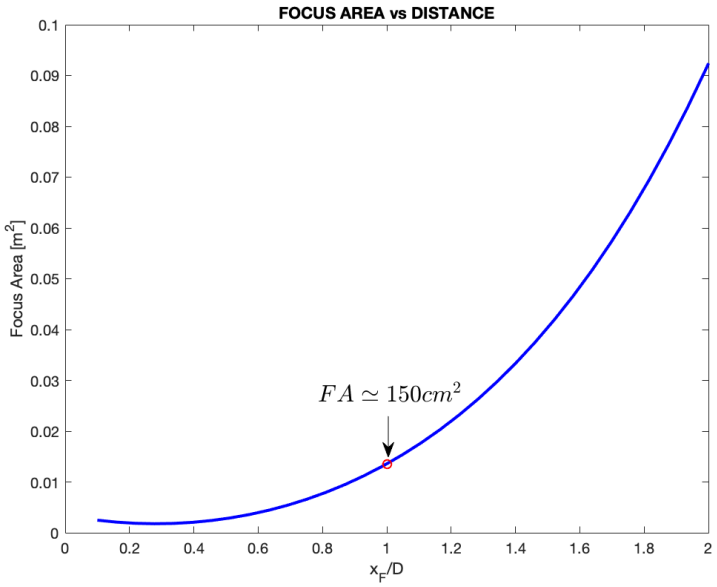

Figure 5.1: Example of RIS dimensioning fixing the bound on the FA.

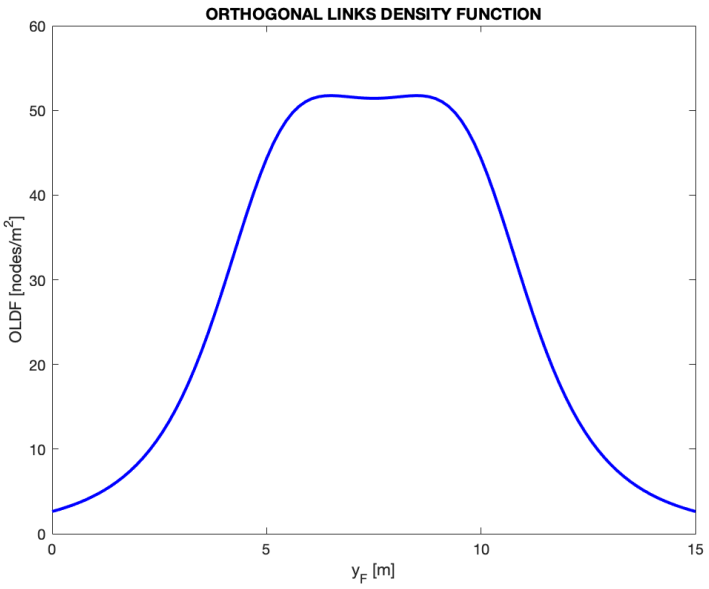

Figure 5.2: Orthogonal Links Density Function.

constant at 50 links per square meter which is a remarkable result because it represents the orthogonal links density RIS can establish with devices. It is

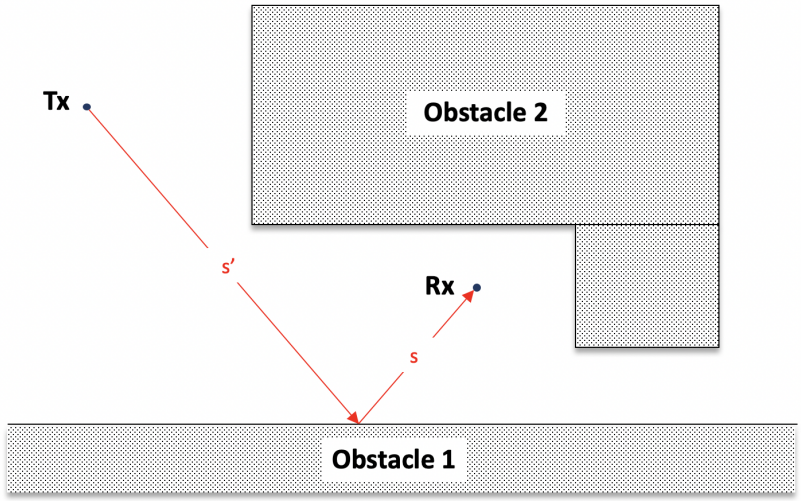

Figure 5.3: Communication in NLOS condition without RIS.

worth noting that this achievement is confined by the limits of the 1D-RIS, nevertheless the use of MTM-based technology, like RISs, could solve the main problems that Industry 4.0 requires to face up to.

In the following a numerical example is provided by applying the Eq. (5.2) above discussed

$$C = l_x \int_{\gamma} \mathcal{A}(y)dy = 0.1 \int_{0}^{15} \mathcal{A}(y)dy \simeq 44 \text{ nodes}$$

where C is the number of orthogonal connections, l_x is the side of the square representing the area of the devices along the x-axis, γ is the integration range along the y-axis and the integral is numerically evaluated.

In the next section a novel approach has been introduced, until now RISs have been used to perform the robustness in communication systems in LOS conditions. The next step is to understand how we can take advantage of RISs in NLOS conditions.

5.2 Enhanced Obstacle Reflections with RISs

5.2.1 Path Gain

Although MTMs are at the beginning of their theoretical discussion, several ideas for applications already emerged. In Chapter 3 an example of performing smart radio environments in LOS conditions with RISs have been

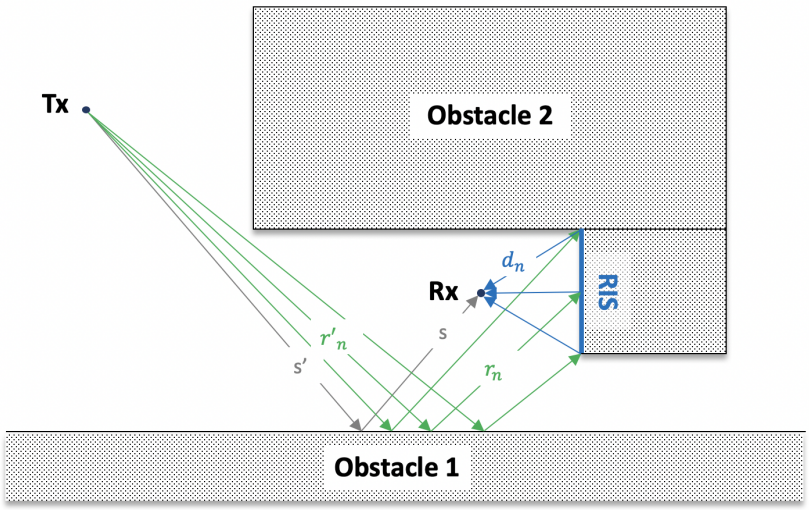

Figure 5.4: Communication in NLOS condition with RIS.

investigated and results are remarkable. In this section a further step is made with the purpose to understand the potential also in NLOS conditions.

In Fig. (5.3) a new scenario is proposed. The receiver is reached only by means of reflections. The presence of a obstacle puts the receiver in NLOS conditions, so the only way to create a link between transmitter and receiver is through ground reflection exploitation. Changing the prospective, this scenario can be used not only to describe ground reflections scenario, but also in micro-cellular scenarios which are quite common in dense urban environments where instead of ground we can have walls participating to the reflection of the EM wave.
For the sake of simplicity, only the 1D-RIS model has been considered and taking advantage of the Images Theorem, the electric field expression in presence of reflection is

$$\vec{E}(R_x) = \Gamma \vec{E}_0(\theta_i, \phi_i) \frac{e^{-j\beta\xi}}{\xi} \tag{5.3}$$

where $\vec{E}_0(\theta_i, \phi_i)$ is the electric field emitted in the ξ direction, $\xi = (s + s')$ is the total length of the communication path where s' and s are represented in Fig.(5.3), and Γ is the reflection coefficient of the obstacle.

A change in the scenario is introduced by adding a RIS in the profile of obstacle 2 (see Fig.(5.4)). Similarly as done in the scenario without RIS, the electric field is

$$\vec{E}_{RIS}(R_x) = \sum_{n=0}^{N-1} \vec{E}_n(RIS) \frac{e^{-j\beta\left[d_n - \frac{\delta_n}{\beta}\right]}}{d_n}$$

where $\vec{E}_n(RIS)$ is the electric field evaluated for the $n-th$ meta-atom composing the RIS and δ_n is the phase delay profile applied to the RIS. Since the RIS is not a point object, it encounters N rays reflecting from the Obstacle 1 and for each of them the reflection coefficient is applied. Assuming an homogeneous material for the obstacle, the reflection coefficient is constant independently of the impinging point. Similarly as done previously with ξ, defining $z_n = (r'_n + r_n)$, the electric field equation for each of the N rays can be the following

$$\vec{E}_n(RIS) = \Gamma \vec{E}_0(\theta_n, \phi_n) \frac{e^{-j\beta z_n}}{z_n}.$$

By means of the above considerations, defining $\Delta_n = [d_n - \delta_n/\beta]$ and assuming the RIS lossles, a new equation can be obtained for the electric field in the receiver

$$\vec{E}_{RIS}(R_x) = \Gamma \sum_{n=0}^{N-1} \vec{E}_0(\theta_n, \phi_n) \frac{e^{-j\beta[\Delta_n + z_n]}}{d_n z_n}. \tag{5.4}$$

In order to simplify the math, the initial electric field $\vec{E}_0(\theta_n, \phi_n)$ is considered constant and equal to its magnitude. In fact, according with the parallel-ray approximation, the distance between the incident point on the obstacle and the transmitter is high enough to consider the wave front locally plane. The electric field can be assumed constant over all the incident region then the Equations (5.3) , (5.4) can be rewritten as:

$$\vec{E}(R_x) = \Gamma |\vec{E}_0| \frac{e^{-j\beta\xi}}{\xi};$$
$$\vec{E}_{RIS}(R_x) = \Gamma |\vec{E}_0| \sum_{n=0}^{N-1} \frac{e^{-j\beta[\Delta_n + z_n]}}{d_n z_n}.$$

The following expression defines the path gain (PG) as

$$PG = \left| \frac{\vec{E}_{RIS}(R_x) + \vec{E}(R_x)}{\vec{E}(R_x)} \right|^2 = \left| 1 + \xi \sum_{n=0}^{N-1} \frac{e^{-j\beta[\Delta_n + z_n - \xi]}}{d_n z_n} \right|^2 \tag{5.5}$$

where the PG describes numerically the advantage adopting RIS compared to the scenario without RIS. Assuming $\xi \approx z_n$ by using the parallel-ray approximation, a new relation is obtained

$$PG \approx \left| 1 + \sum_{n=0}^{N-1} \frac{e^{-j\beta[\Delta_n + z_n - \xi]}}{d_n} \right|^2 .$$

Imposing $\Delta_n + z_n - \xi \triangleq 0$ in order to guarantee a coherent summation on the receiver, the phase delay profile of the RIS is obtained

$$\delta_n = \beta(d_n + z_n - \xi) \tag{5.6}$$

then injecting Eq. (5.6) in Eq.(5.5) a new equation is derived

$$PG = \left| 1 + \sum_{n=0}^{N-1} \frac{1}{d_n} \right|^2 \tag{5.7}$$

In this section the PG of a NLOS connection through reflections on a lossless RIS has been introduced. PG is an important figure of merit to evaluate the performances of the system. In order to better understand this technology, in the next section a numerical example has been presented.

5.2.2 Example: A Numerical Approach for PG

Under the aforementioned link distance condition, Eq. (5.7) can be used to determine the PG which describes the advantage of using RIS in a scenario like the following.
Fig. (5.5) represents the propagation environment where the following dimensions have been considered:

- $f = 28\,GHz$, is the carrier frequency;
- N, is the number of meta-atoms composing the RIS;
- $d = \lambda/2$, is the distance between meta-atoms;
- $y_1 = 40\,m$, is the transmitter coordinate respect to the ground;
- $y_3 = 20\,m$, is the RIS coordinate respect to the ground;
- $x = 1000\,m$, is the distance between transmitter and receiver;
- $\delta x = 2\,m$, is the distance between receiver and the RIS.

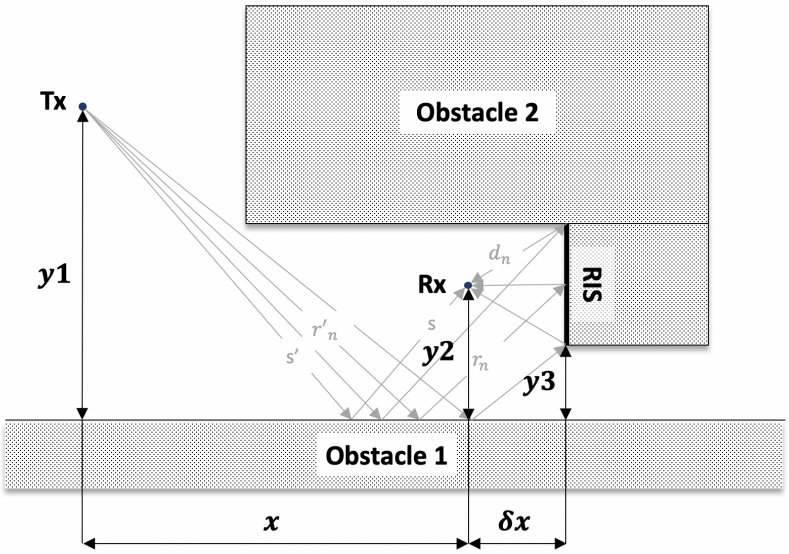

Figure 5.5: Example of propagation environment.

The receiver position y_2 is located at the center of the RIS and it varies as a function of the RIS's dimension. The RIS is considered lossless with variable size between 0 to $5\,m$ and the transmitted signal is monochromatic emitted by an isotropic antenna. In this example the purpose is to evaluate the PG as a function of the RIS's size: N.

By the use of trigonometric considerations, observing the Fig. (5.5) the following equations have been obtained

$$D_{RIS} = d(N-1)$$
$$d_n = \sqrt{\delta_x^2 + \left(\frac{D_{RIS}}{2} - nd\right)^2}$$

where D_{RIS} is the RIS's size and n is the n-th element composing the RIS.

Fig. (5.6) is obtained after simulations and it shows an high increment in RIS's size does not lead into an equivalent advantage in terms of PG. On the contrary, for smaller RIS the PG increases rapidly. It is worth noting that the above discussed mathematical model is bounded to the dimensions of the system. In fact for low distances between transmitter and receiver the local plane wave approximation ceases to be valid. Another limit is relate to the RIS's size because it can not be assumed too high in order to avoid violating the principle of energy conservation. In fact assuming $N \to \infty$ the

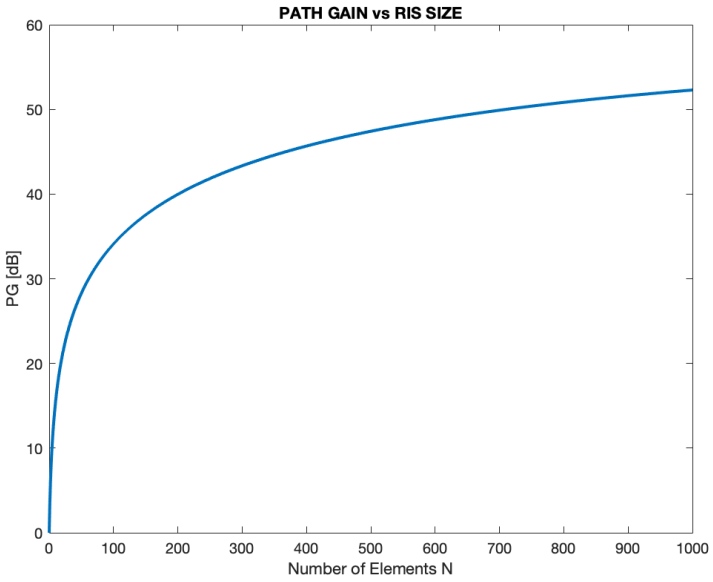

Figure 5.6: Path gain as a function of RIS's size.

PG seems to grow to infinitive. This is an oddity due to the mathematical model which does not take in account the geometry of the system. As a matter of fact the geometry itself limits the RIS's size in order to guarantee the NLOS condition between transmitter and receiver.

Conclusions

MTMs are an emerging class of materials and their use can be extended to several fields of application among communications, data processing, identification, etc. In this thesis we have focused on the possibility to use MTMs to convert the environment in a programmable space called smart radio environment by tailoring the way EM waves are reflected which translates into a control of the propagation paths reflection. To achieve this objective, we have described mathematically the EM behavior of a special kind of programmable MTS called RIS and then we have introduced two algorithms, one numerical, the other analytical by assuming a 1D model for the RIS. The solutions provided by our algorithms allowed us to derive the FP, which represents the point where the EM field exploiting the RIS is summed coherently, and the FA, which represents the ability of the RIS to focus the electric field in the FP. Then we have extended the 1D-RIS mathematical model to the 2D-RIS obtaining a 3D representation of the field propagation. Finally we have compared the results obtained from numerical and analytical algorithms to assess which one provides a better accuracy in FA computation.

Subsequently, starting from the mathematical characterization for RISs, we have verified that when the size of the RIS is comparable with the distances involved, the RIS improves its focusing ability of the EM field, thus opening the possibility of realizing a very large number of orthogonal connections. This feature is especially useful in IIoT scenarios where we need to manage massive sensor connectivity in noisy environments.

List of Tables

List of Figures

Bibliography

[1] Ian F. Akyildiz, Ahyoung Lee, Pu Wang, Min Luo, and Wu Chou. A roadmap for traffic engineering in software defined networks. *Computer Networks*, 71:1–30, 2014.

[2] Ian F. Akyildiz, Shuai Nie, Shih Chun Lin, and Manoj Chandrasekaran. 5G roadmap: 10 key enabling technologies. *Computer Networks*, 106:17–48, 2016.

[3] Andrea Alù and Nader Engheta. Performing Mathematical Operations with Metamaterials. *Science (New York, N.Y.*, (January):160–164, 2014.

[4] Ertugrul Basar, Marco Di Renzo, Julien De Rosny, Merouane Debbah, Mohamed-Slim Alouini, and Rui Zhang. Wireless Communications Through Reconfigurable Intelligent Surfaces. *IEEE Access*, 7(June):116753–116773, 2019.

[5] I. A. Buriak, V. O. Zhurba, G. S. Vorobjov, V. R. Kulizhko, O. K. Kononov, and Oleksandr Rybalko. Metamaterials: Theory, classification and application strategies (review). *Journal of Nano- and Electronic Physics*, 8(4):1–11, 2016.

[6] Wikipedia contributors. Near and far field — {Wikipedia}{,} The Free Encyclopedia, 2019.

[7] Filippo Costa, Simone Genovesi, and Agostino Monorchio. Chipless RFIDs by using metasurfaces. *8th European Conference on Antennas and Propagation, EuCAP 2014*, (EuCAP):2384–2388, 2014.

[8] Tie Jun Cui, Mei Qing Qi, Xiang Wan, Jie Zhao, Qiang Cheng, Kyu Tae Lee, Jae Yong Lee, Sungyong Seo, L. Jay Guo, Zichen Zhang, Zheng You, and Daping Chu. Coding metamaterials, digital metamaterials and programmable metamaterials. *Light: Science and Applications*, 3(10), 2014.

[9] Nader Engheta and Richard W. Ziolkowski. *Metamaterials: Physics and engineering exploartion*, volume 37. 1986.

[10] Nader Engheta and Richard W. Ziolkowski. A positive future for double-negative metamaterials. *IEEE Transactions on Microwave Theory and Techniques*, 53(4 II):1535–1555, 2005.

[11] Yijun Feng, Bo Zhu, Junming Zhao, and Tian Jiang. Dynamic control of electromagnetic wave polarization and phase through active metasurfaces. *Proceedings of 3rd Asia-Pacific Conference on Antennas and Propagation, APCAP 2014*, pages 1069–1071, 2014.

[12] M. E. Jalil, Noor Asmawati Samsuri, Mohammad Kamal A. Rahim, and R. Dewan. Compact chipless RFID metamaterial based structure using textile material. *2015 International Symposium on Antennas and Propagation, ISAP 2015*, pages 1–4, 2016.

[13] Avish Karmakar, Naiwrita Dey, Tapadyuti Baral, Manojeet Chowdhury, and Md Rehan. Industrial internet of things: A review. *2019 International Conference on Opto-Electronics and Applied Optics, Optronix 2019*, pages 1–6, 2019.

[14] H Kwon, D Sounas, and A Alù. Nonlocal Metasurfaces Performing Analog Mathematical Operations. In *2018 IEEE International Symposium on Antennas and Propagation USNC/URSI National Radio Science Meeting*, pages 769–770, jul 2018.

[15] Huan Li, Dexin Ye, Fazhong Shen, Bin Zhang, Yongzhi Sun, Weiqiang Zhu, Changzhi Li, and Lixin Ran. Reconfigurable diffractive antenna based on switchable electrically induced transparency. *IEEE Transactions on Microwave Theory and Techniques*, 63(3):925–936, 2015.

[16] Christos Liaskos, Shuai Nie, Ageliki Tsioliaridou, Andreas Pitsillides, Sotiris Ioannidis, and Ian Akyildiz. A New Wireless Communication Paradigm through Software-Controlled Metasurfaces. *IEEE Communications Magazine*, 56(9):162–169, 2018.

[17] C Liu, Z Dutton, C.˜H. Behroozi, and L.˜V. Hau. Observation of coherent optical information storage in an atomic medium using halted light pulses. *nat*, 409:490–493, jan 2001.

[18] Francesco Monticone, Andrea Alù, Vincenzo Galdi, and Nader Engheta. 'Computing metasurfaces' to perform mathematical operations. *IEEE*

Antennas and Propagation Society, AP-S International Symposium (Digest), pages 27–28, 2014.

[19] Toshihiro Nakanishi, Takehiro Otani, Yasuhiro Tamayama, and Masao Kitano. Storage of electromagnetic waves in a metamaterial that mimics electromagnetically induced transparency. *Physical Review B - Condensed Matter and Materials Physics*, 87(16), 2013.

[20] Paolo Nepa and Alice Buffi. Near-field-focused microwave antennas: Near-field shaping and implementation. *IEEE Antennas and Propagation Magazine*, 59(3):42–53, 2017.

[21] K. Ntontin, M. Di Renzo, J. Song, F. Lazarakis, J. de Rosny, Dinh Thuy T. Phan-Huy, O. Simeone, R. Zhang, Merouane Debbah, Geoffroy Lerosey, Mathias Fink, S. Tretyakov, and S. Shamai. Reconfigurable Intelligent Surfaces vs. Relaying: Differences, Similarities, and Performance Comparison. *Eurasip Journal on Wireless Communications and Networking*, 2019(1):1–7, 2019.

[22] Marco Di Renzo, Merouane Debbah, Dinh Thuy Phan-Huy, Alessio Zappone, Mohamed Slim Alouini, Chau Yuen, Vincenzo Sciancalepore, George C. Alexandropoulos, Jakob Hoydis, Haris Gacanin, Julien de Rosny, Ahcene Bounceur, Geoffroy Lerosey, and Mathias Fink. Smart radio environments empowered by reconfigurable AI meta-surfaces: an idea whose time has come. *Eurasip Journal on Wireless Communications and Networking*, 2019(1), 2019.

[23] Giuseppe Ruvio. State-of-the-art of Metamaterials: Characterization, Realization and Applications. *Studies in Engineering and Technology*, 1(2):38, 2014.

[24] Krishnasamy T. Selvan and Ramakrishna Janaswamy. Fraunhofer and Fresnel Distances : Unified derivation for aperture antennas. *IEEE Antennas and Propagation Magazine*, 59(4):12–15, 2017.

[25] C. E. Shannon. A Mathematical Theory of Communication. *The Bell System Technical Journal*, 27(3):379 – 423, 1948.

[26] A. Silva, F. Monticone, G. Castaldi, V. Galdi, A. Alu, and N. Engheta. Metamaterial-based analog computing. *2014 3rd Mediterranean Photonics Conference, MePhoCo 2014*, pages 5–7, 2014.

[27] Norbert Wiener. *Cybernetics, or Control and Communication in the Animal and the Machine*. Number 2. 2nd - 1961 edition, 1948.

[28] Huanhuan Yang, Xiangyu Cao, Fan Yang, Jun Gao, Shenheng Xu, Maokun Li, Xibi Chen, Yi Zhao, Yuejun Zheng, and Sijia Li. A programmable metasurface with dynamic polarization, scattering and focusing control. *Scientific Reports*, 6(October):1–11, 2016.